NASA / CR-2001-211245

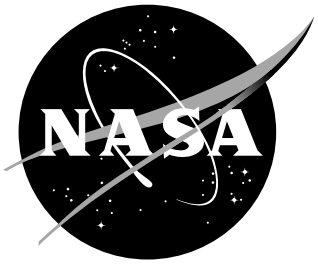

Turbofan Duct Propagation Model

Justin H. Lan
The Boeing Company, Seattle, Washington

December 2001

The NASA STI Program Office ... in Profile

Since its founding, NASA has been dedicated to the advancement of aeronautics and space science. The NASA Scientific and Technical Information (STI) Program Office plays a key part in helping NASA maintain this important role.

The NASA STI Program Office is operated by Langley Research Center, the lead center for NASA's scientific and technical information. The NASA STI Program Office provides access to the NASA STI Database, the largest collection of aeronautical and space science STI in the world. The Program Office is also NASA's institutional mechanism for disseminating the results of its research and development activities. These results are published by NASA in the NASA STI Report Series, which includes the following report types:

- TECHNICAL PUBLICATION. Reports of completed research or a major significant phase of research that present the results of NASA programs and include extensive data or theoretical analysis. Includes compilations of significant scientific and technical data and information deemed to be of continuing reference value. NASA counterpart of peer-reviewed formal professional papers, but having less stringent limitations on manuscript length and extent of graphic presentations.

- TECHNICAL MEMORANDUM. Scientific and technical findings that are preliminary or of specialized interest, e.g., quick release reports, working papers, and bibliographies that contain minimal annotation. Does not contain extensive analysis.

- CONTRACTOR REPORT. Scientific and technical findings by NASA-sponsored contractors and grantees.

- CONFERENCE PUBLICATION. Collected papers from scientific and technical conferences, symposia, seminars, or other meetings sponsored or co-sponsored by NASA.

- SPECIAL PUBLICATION. Scientific, technical, or historical information from NASA programs, projects, and missions, often concerned with subjects having substantial public interest.

- TECHNICAL TRANSLATION. English-language translations of foreign scientific and technical material pertinent to NASA's mission.

Specialized services that complement the STI Program Office's diverse offerings include creating custom thesauri, building customized databases, organizing and publishing research results ... even providing videos.

For more information about the NASA STI Program Office, see the following:

- Access the NASA STI Program Home Page at ***http://www.sti.nasa.gov***

- E-mail your question via the Internet to help@sti.nasa.gov

- Fax your question to the NASA STI Help Desk at (301) 621-0134

- Phone the NASA STI Help Desk at (301) 621-0390

- Write to:
  NASA STI Help Desk
  NASA Center for AeroSpace Information
  7121 Standard Drive
  Hanover, MD 21076-1320

NASA / CR-2001-211245

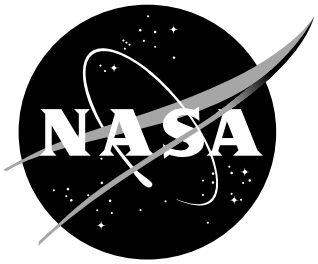

Turbofan Duct Propagation Model

Justin H. Lan
The Boeing Company, Seattle, Washington

National Aeronautics and
Space Administration

Langley Research Center
Hampton, Virginia 23681-2199

Prepared for Langley Research Center
under Contract NAS1-97040, Task 5

December 2001

Acknowledgments

The author would like to acknowledge Mike Jones and Maureen Tracy for their helpful discussions on the NASA Langley Grazing Flow Impedance Tube. Gerry Bielak and John Premo deserve thanks for their many suggestions and discussions on acoustic lining, duct acoustic propagation, and phased arrays. I would like to acknowledge Joe Posey for his role as contract monitor. Bob Dougherty deserves special acknowledgment for his role as the original author and developer of the CDUCT code, and his role as a general mentor.

Available from:

NASA Center for AeroSpace Information (CASI)
7121 Standard Drive
Hanover, MD 21076-1320
(301) 621-0390

National Technical Information Service (NTIS)
5285 Port Royal Road
Springfield, VA 22161-2171
(703) 605-6000

Abstract

The CDUCT code utilizes a parabolic approximation to the convected Helmholtz equation in order to efficiently model acoustic propagation in acoustically treated, complex shaped ducts. The parabolic approximation solves one-way wave propagation with a marching method which neglects backwards reflected waves. The derivation of the parabolic approximation is presented. Several code validation cases are given. An acoustic lining design process for an example aft fan duct is discussed. It is noted that the method can efficiently model realistic three-dimension effects, acoustic lining, and flow within the computational capabilities of a typical computer workstation.

Table of Contents

List of Tables

List of Figures

List of Symbols

$\vec{a}_i$	unit vectors in $\vec{\xi}_i$ directions
c	speed of sound
h	duct dimensions
h_1	distance associated with a unit change in ξ_1
h_2	distance associated with a unit change in ξ_2
h_3	distance associated with a unit change in ξ_3
i	index or imaginary number
j	index
k	wave number or integer
k_z	wave number
m	spinning mode order
n	harmonic index
t	time
v	flow velocity magnitude
$\vec{v}$	flow velocity vector
w	duct dimension
x	Cartesian coordinate
x_1	Cartesian coordinate
x_2	Cartesian coordinate
x_3	Cartesian coordinate
y	Cartesian coordinate
z	Cartesian coordinate
A	specific admittance
A_{mn}	mode constants

A_0 matrix

A_1 matrix or model coefficient

A_2 model coefficient

B number of rotor blades

BF beamform expression

BPF blade passage frequency

CRPM corrected revolution per minute

EPNL effective perceived noise level

G vector

I_1 index

I_3 acoustic intensity

L duct dimension

M Mach number

N_1 maximum grid index number

P matrix

PNLT tone corrected perceived noise level

Q matrix

R specific resistance or radial coordinate

V number of stators

W acoustic power

X specific reactance or axial coordinate

α matrix term for forward traveling waves

β coupling term

δ matrix term for backward traveling waves

γ coupling term

ϕ acoustic potential

ω angular frequency

ξ_1 orthogonal curvilinear coordinate

ξ_2 orthogonal curvilinear coordinate

ξ_3 orthogonal curvilinear coordinate

ψ^+ acoustic potential for forward traveling waves

ψ^- acoustic potential for backward traveling waves

ψ_0^+ acoustic velocity potential below an infinitely thin boundary layer

Φ flow velocity potential

1.0 Introduction

Aft fan noise refers to acoustic energy that is generated by the fan of a turbofan engine and propagates downstream through the aft fan duct and eventually radiates to the farfield. Figure 1 shows the aft fan duct geometry of a typical turbofan engine. Aft fan noise radiation accounts for a large portion of the community noise generated by modern commercial transport aircraft. One of the most important techniques for controlling aft fan noise is the use of acoustic lining. The design of this lining depends on accurately modeling the acoustic propagation through the complex shaped duct. The CDUCT code was developed under the NASA Advanced Subsonic Transport (AST) Contract NAS1-97040 to efficiently model duct acoustic propagation and help design acoustic lining systems.

1.1 CDUCT Code

Several techniques exist for solving duct acoustic propagation problems. These include mode methods [1], finite elements [2], computational aeroacoustics [3], and ray acoustics [4]. It is noted that the typical mode methods do not account for important details in geometry. Finite element and computational aeroacoustics techniques are computationally slow which is not ideal for optimization and design problems. Furthermore, ray acoustic techniques are not accurate for the typical aft fan duct geometry at frequencies of interest.

The CDUCT code is based on a parabolic approximation to the convected Helmholtz equation. The approximation simplifies the problem by neglecting reflections that couple downstream propagating waves to upstream propagating waves. The problem transforms into solving one-way wave propagation, which can be accomplished with a computationally fast marching method. The method can account for three-dimensional effects, acoustic lining, and flow within the computational capabilities of a typical computer workstation.

1.2 Outline and Summary of Work

The primary objective of this research is to validate the turbofan duct propagation code, CDUCT, and utilize the code to design and optimize aft fan duct acoustic systems. The CDUCT code is validated with both analytical solutions and experimental data to establish its accuracy and explore its strengths and limitations. Optimization of acoustic lining impedance distributions is demonstrated for the aft fan duct of a typical modern high bypass ratio engine. A detailed advanced liner design is then developed for an example aft fan duct and its performance is compared to current production technology. A unique application of CDUCT is also presented, where measurements from a phased array system mounted to an inflow control device are combined with CDUCT predictions to result in a mode measurement system. This mode measurement system was tested at the NASA Glenn Active Noise Control Fan Facility and validated with the rotating rake system.

Section 2 describes the CDUCT parabolic approximation. Section 3 presents the CDUCT validation results. Section 4 describes the CDUCT impedance optimization and lining design. Section 5 describes the CDUCT mode measurement system. Finally, Section 6 presents conclusions and recommendations.

1.0 CDUCT Parabolic Approximation

The CDUCT code is based on a parabolic approximation to the convected Helmholtz equation in an orthogonal curvilinear coordinate system [5,6]. The convected Helmholtz equation is written as a coupled, first order system of partial differential equations. The coupling terms representing reflections are neglected which results in a pair of one-way propagation equations. The propagation equation representing forward going waves are solved with a marching method. The resulting method also accounts for the transverse boundary conditions that represent the impedance surface of the duct and the effect of an infinitely thin flow boundary layer.

2.1 Governing Equation

The acoustic velocity potential is assumed to obey the convected wave equation

$$\frac{1}{c^2} D_t^2 \phi = \nabla^2 \phi \tag{1}$$

where ϕ is the acoustic velocity potential, c is the speed of sound, and the total derivative is

$$D_t = \frac{\partial}{\partial t} + \vec{v} \cdot \nabla = -i\omega + \vec{v} \cdot \nabla \tag{2}$$

where t is time, $\vec{v}$ is the flow velocity vector, ω is angular frequency and i is the imaginary number. An acoustic time dependence of $e^{-i\omega t}$ is assumed. Let $\xi_1 \in [0,\pi], \xi_2 \in [0,\pi], \xi_3 \in [0,1]$ be a system of orthogonal curvilinear coordinates such that the ξ_3 coordinate lines are parallel to the flow. The Laplacian operator in the orthogonal curvilinear coordinate system can be written as

$$\nabla^2 \phi = \nabla_\perp^2 \phi + \frac{1}{h_1 h_2 h_3} \frac{\partial}{\partial \xi_3} \left(\frac{h_1 h_2}{h_3} \frac{\partial \phi}{\partial \xi_3} \right) \tag{3}$$

where the transverse Laplacian, $\nabla_\perp^2 \phi$, is written as

$$\nabla_\perp^2 \phi = \frac{1}{h_1 h_2 h_3} \left[\frac{\partial}{\partial \xi_1} \left(\frac{h_2 h_3}{h_1} \frac{\partial \phi}{\partial \xi_1} \right) + \frac{\partial}{\partial \xi_2} \left(\frac{h_1 h_3}{h_2} \frac{\partial \phi}{\partial \xi_2} \right) \right] \tag{4}$$

and

$$h_i = \left[\sum_j \left(\frac{\partial x_j}{\partial \xi_i} \right)^2 \right]^{1/2} \qquad \text{i} = 1,3 \quad \text{j} = 1,3 \tag{5}$$

represents the distance associated with a unit change in ξ_i, and the x_j represent a Cartesian coordinate

system [7]. The gradient is written as

$$\nabla\phi = \sum_{i=1}^{3} \vec{a}_i \frac{1}{h_i}\frac{\partial\phi}{\partial\xi_i} \tag{6}$$

where $\vec{a}_i$ are the unit vectors in the $\vec{\xi}_i$ directions. Substituting Eqns. (2) and (3) into Eqn. (1) and using the assumption that $\vec{v}$ is parallel to $\vec{\xi}_3$ results in

$$\frac{1-M^2}{h_3}\frac{\partial}{\partial\xi_3}\left(\frac{1}{h_3}\frac{\partial\phi}{\partial\xi_3}\right) = \left[-\frac{1}{h_1h_2h_3}\frac{\partial}{\partial\xi_3}(h_1h_2) - 2ikM + \frac{M}{h_3}\frac{\partial M}{\partial\xi_3}\right]\frac{1}{h_3}\frac{\partial\phi}{\partial\xi_3} - \nabla_\perp^2\phi - k^2\phi \tag{7}$$

where the Mach number, M, is

$$M = \frac{v}{c} \tag{8}$$

and the wave number, k, is

$$k = \frac{\omega}{c} \tag{9}$$

Eqn. (7) can be expressed as a system of first order equations through a change of variables. First, Eqn. (7) is written as

$$\frac{1-M^2}{h_3}\frac{\partial}{\partial\xi_3}\begin{bmatrix}\phi\\ \frac{1}{h_3}\frac{\partial\phi}{\partial\xi_3}\end{bmatrix} = \begin{bmatrix}0 & 1-M^2\\ -k^2-\nabla_\perp^2 & -2ikM - \frac{1}{h_1h_2h_3}\frac{\partial}{\partial\xi_3}(h_1h_2) + \frac{M}{h_3}\frac{\partial M}{\partial\xi_3}\end{bmatrix}\begin{bmatrix}\phi\\ \frac{1}{h_3}\frac{\partial\phi}{\partial\xi_3}\end{bmatrix} \tag{10}$$

Let the matrix in Eqn. (10) be expressed as $A_0 + A_1$ where

$$A_0 = \begin{bmatrix}0 & 1-M^2\\ -k^2 & -2ikM\end{bmatrix} \tag{11}$$

and

$$A_1 = \begin{bmatrix}0 & 0\\ -\nabla_\perp^2 & -\frac{1}{h_1h_2h_3}\frac{\partial}{\partial\xi_3}(h_1h_2) + \frac{M}{h_3}\frac{\partial M}{\partial\xi_3}\end{bmatrix} \tag{12}$$

Let P be a matrix whose columns are the eigenvectors of A_0

$$P = \begin{bmatrix} 1 & 1 \\ \frac{ik}{1+M} & -\frac{ik}{1-M} \end{bmatrix} \tag{13}$$

and define the new dependent variables ψ^+ and ψ^- by

$$\begin{bmatrix} \phi \\ \frac{1}{h_3}\frac{\partial \phi}{\partial \xi_3} \end{bmatrix} = P \begin{bmatrix} \psi^+ \\ \psi^- \end{bmatrix} \tag{14}$$

By using Eqns. (11), (12), and (14), Eqn. (10) can be rewritten as the system of first order equations

$$\frac{\partial}{\partial \xi_3}\begin{bmatrix} \psi^+ \\ \psi^- \end{bmatrix} = \begin{bmatrix} \alpha & \beta \\ \gamma & \delta \end{bmatrix}\begin{bmatrix} \psi^+ \\ \psi^- \end{bmatrix} \tag{15}$$

where the matrix terms are

$$\begin{bmatrix} \alpha & \beta \\ \gamma & \delta \end{bmatrix} = \frac{h_3}{1-M^2} P^{-1} A_0 P + \frac{h_3}{1-M^2} P^{-1} A_1 P - P^{-1}\frac{\partial P}{\partial \xi_3} \tag{16}$$

and α and δ are terms associated with the forward and backward going waves, respectively, and β and γ are coupling terms. If the coupling terms are neglected, the forward propagation equation is

$$\frac{\partial \psi^+}{\partial \xi_3} = \alpha \psi^+ \tag{17}$$

where

$$\alpha = \frac{h_3 ik}{1+M} - \frac{h_3}{2ik}\nabla_\perp^2 - \frac{1}{1+M}\frac{1}{2h_1 h_2}\frac{\partial}{\partial \xi_3}(h_1 h_2) + \frac{1}{2(1+M)}\frac{\partial M}{\partial \xi_3} \tag{18}$$

The steady flow velocity is given by

$$\vec{v} = -\nabla \Phi \tag{19}$$

where Φ is the velocity potential, which obeys the Laplace equation

$$\nabla^2 \Phi = 0 \tag{20}$$

Since the flow is aligned with ξ_3, Eqn. (20) reduces to

$$\frac{\partial}{\partial \xi_3}\left(h_1 h_2 M\right) = 0 \tag{21}$$

Using Eqn. (21), Eqn. (17) results in the parabolic approximation

$$\frac{\partial \psi^+}{\partial \xi_3} = \frac{h_3 ik}{1+M}\psi^+ - \frac{h_3}{2ik}\nabla_\perp^2 \psi^+ - \frac{1}{2h_1 h_2}\frac{\partial}{\partial \xi_3}\left(h_1 h_2\right)\psi^+ \tag{22}$$

2.2 Impedance Boundary Condition

The transverse boundary conditions of the duct are assumed to be locally reacting impedance surfaces, which are out of the flow and are written as

$$\pm \frac{1}{h_j}\frac{\partial \psi_0^+}{\partial \xi_j} = ikA\psi_0^+ \tag{23}$$

where ψ_0^+ is the acoustic velocity potential below an infinitely thin boundary layer, and A is the specific admittance. The negative sign corresponds to $\xi_j = 0$ and the positive sign corresponds to $\xi_j = \pi$ for j = 1 and 2. The acoustic pressure and the normal acoustic particle displacement are continuous across the infinitely thin boundary layer and are written as

$$D_t \psi^+ = \frac{\partial \psi_0^+}{\partial t} \tag{24}$$

and

$$D_t^{-1}\frac{\partial \psi^+}{\partial \xi_j} = \left(\frac{\partial}{\partial t}\right)^{-1}\frac{\partial \psi_0^+}{\partial \xi_j} \tag{25}$$

By using the acoustic time dependence as $e^{-i\omega t}$ and eliminating ψ_0^+, the impedance boundary conditions can be written as

$$\frac{\partial \psi^+}{\partial \xi_j} = \mp ik\left(-i + \frac{M}{kh_3}\frac{\partial}{\partial \xi_3}\right)\left(h_j A\left[-i + \frac{M}{kh_3}\frac{\partial}{\partial \xi_3}\right]\psi^+\right) \tag{26}$$

The presence of the derivatives with respect to ξ_3 is numerically awkward. In order to simplify the boundary conditions, the first term in the parabolic equation, Eqn. (22), is used for the derivatives of

acoustic potential and the derivatives of Mach number are neglected which results in the approximation

$$\frac{\partial \psi^+}{\partial \xi_j} = \pm ikA \frac{h_j}{(1+M)^2} \psi^+ \mp \frac{1}{h_3} \frac{h_j M}{1+M} \frac{\partial A}{\partial \xi_3} \psi^+ \tag{27}$$

2.3 Marching Method

The parabolic approximation, Eqn. (22), is a system of ordinary differential equations, and can be solved with a marching method that progressively advances the solution in ξ_3. The classical 4th order Runge-Kutta method is used for its accuracy and ease of implementation. The initial acoustic velocity potential that describes the noise source at the entrance of the duct must be specified. Note that this noise source description is only rarely known and thus approximations must be used such as a planewave source, gaussian distribution, or a series of acoustic duct modes.

The transverse derivatives in Eqn. (22) are evaluated by a pseudospectral approach. This method models the values of ψ^+ at the grid points by a series of sine and cosine functions. The derivatives are determined from the model. Let ξ_1 and ξ_2 be discretized on a uniformly spaced grid from 0 to π. The model for ψ^+ in the ξ_1 direction can be written as

$$\psi^+ = A_1 \sin(\xi_1) + A_2 \sin(2\xi_1) + \sum_{I_1=0}^{N_1-1} B_{I_1} \cos(I_1 \xi_1) \tag{28}$$

where A_1, A_2, and B_{I_1} are the model coefficients, and N_1 is the maximum grid index number in the ξ_1 direction. The boundary conditions from Eqn. (27) are used to evaluate the A_1 and A_2 coefficients and a fast Fourier transform method is used to evaluate the B_{I_1} coefficients. Once the model coefficients are determined, the derivatives are calculated from

$$\frac{\partial \psi^+}{\partial \xi_1} = A_1 \cos(\xi_1) + 2A_2 \cos(2\xi_1) - \sum_{I_1=0}^{N_1-1} I_1 B_{I_1} \sin(I_1 \xi_1) \tag{29}$$

and

$$\frac{\partial^2 \psi^+}{\partial \xi_1^2} = -A_1 \sin(\xi_1) - 4A_2 \sin(2\xi_1) - \sum_{I_1=0}^{N_1-1} I_1^2 B_{I_1} \cos(I_1 \xi_1) \tag{30}$$

The same procedure is used to evaluate the derivatives in the ξ_2 direction. Once these transverse derivatives are determined, the right-hand-side of Eqn. (22) is complete, and the solution can be marched forward.

It is noted that the parabolic approximation in Eqn. (22) is accurate for waves propagating at small angles to the ξ_3 direction [5]. In an acoustically treated duct, this small angle limitation should not be very important since larger angle waves are more easily absorbed by the acoustic lining. Numerical damping in the current parabolic method approximates large angle modes that have decaying solutions for

the full wave equation [5]. The performance of the duct and acoustic treatment is characterized by the acoustic power at each solution plane. The acoustic power, W, can be computed by integrating the intensity

$$W = \iint I_3 h_1 h_2 d\xi_1 d\xi_2 \tag{31}$$

where the intensity expression, I_3, is

$$I_3 = \frac{\rho c M}{4}\left[\left(M^2-1\right)\psi_3^+\psi_3^{+*} + \psi_1^+\psi_1^{+*} + \psi_2^+\psi_2^{+*} + k^2\psi^+\psi^{+*}\right] - \frac{i\rho c k}{4}\left(1-M^2\right)\left(\psi_3^+\psi^{+*} - \psi^+\psi_3^{+*}\right) \tag{32}$$

and

$$\psi_j^+ = \frac{1}{h_j}\frac{\partial\psi^+}{\partial\xi_j} \tag{33}$$

The superscript asterisk indicates a complex conjugate. This intensity expression can be derived from a formula from Reference 8.

2.0 CDUCT Prediction Validation

The CDUCT code is validated with both analytical solutions and experimental data. For the analytical validation, a rigid wall rectangular duct with an acoustic source and uniform flow is modeled with CDUCT. The CDUCT solution is compared with the exact modal solution of the convected one-way Helmholtz equation for the duct. In general, the CDUCT results are very accurate for this analytical test case. For the experimental validation, three different test facilities are modeled with CDUCT. The first facility is the NASA Langley Grazing Flow Impedance Tube [9]. This facility has a rectangular test section and provides a controlled flow and acoustic environment over an acoustic lining test specimen. Only the lowest order planewave mode propagates at the frequencies of interest. The CDUCT results are compared to the measured acoustic field, which is sampled at several points along a duct wall for various flow and acoustic environments. The second and third facilities are a rectangular flow duct studied in Reference 10 and an annular flow duct studied in Reference 11, respectively. For these flow ducts, the CDUCT results are compared to the measured in-duct attenuation for a given acoustic source, lining impedance, and flow. In general, the comparison between CDUCT solutions and experimental data show very favorable results.

3.1 Rigid Wall Rectangular Duct

CDUCT is validated with the analytical solution for a rigid wall rectangular duct with uniform flow. For a rectangular duct with uniform flow in the positive z direction, the convected Helmholtz equation can be written as

$$\left(\frac{\partial^2}{\partial x^2} + \frac{\partial^2}{\partial y^2} + \frac{\partial^2}{\partial z^2} \right) \phi + k^2 \phi + 2ikM \frac{\partial \phi}{\partial z} - M^2 \frac{\partial^2 \phi}{\partial z^2} = 0 \tag{34}$$

where simple harmonic waves of the form $e^{-i\omega t}$ are assumed, ω is the angular frequency, t is time, i is the imaginary number, (x,y,z) are the coordinate axes, ϕ is the acoustic potential, k is the wavenumber, f is the frequency, c is the speed of sound, and M is the uniform Mach number in the z direction. The geometry is shown in Figure 2. The boundary conditions for rigid walls are

$$\frac{\partial \phi}{\partial x}(x = 0, w) = 0 \tag{35}$$

and

$$\frac{\partial \phi}{\partial y}(y = 0, h) = 0 \tag{36}$$

where w and h are duct dimensions defined in Figure 2. Using the method of separation of variables, the solution to Eqn. (34) can be written as

$$\phi(x, y, z) = \sum_{m=0}^{\infty} \sum_{n=0}^{\infty} A_{mn} \cos \frac{m\pi x}{w} \cos \frac{n\pi y}{h} e^{ik_z z} \tag{37}$$

where m and n are mode integers in the x and y directions respectively, A_{mn} are mode constants,

and k_z is

$$k_z = \frac{-kM + \sqrt{k^2 - (1-M^2)\left[\left(\frac{m\pi}{w}\right)^2 + \left(\frac{n\pi}{h}\right)^2\right]}}{1-M^2} \tag{38}$$

Note that when the term under the radical in Eqn. (38) becomes negative, the duct mode decays exponentially (the mode is cut-off). By assuming the acoustic source is a single duct mode of the form

$$\phi(x, y, z=0) = \cos\frac{m\pi x}{w}\cos\frac{n\pi y}{h} \tag{39}$$

the solution, Eqn. (37), can be written as

$$\phi(x, y, z) = \cos\frac{m\pi x}{w}\cos\frac{n\pi y}{h}e^{ik_z z} \tag{40}$$

A duct of dimensions one meter in width and height and two meters in length is used as the validation case (w=1m, h=1m, L=2m). The speed of sound is assumed to be c=340.3 m/s. In order to simulate a hardwall boundary condition in CDUCT, a specific resistance equal to 1000 and zero specific reactance are specified at the wall boundaries. A uniform rectangular computational grid of size 21 X 21 X 41 is used for the CDUCT calculation. For a direct comparison, the analytical solution is computed on the same grid points.

With no flow (M=0.0), the real part of the acoustic potential from the CDUCT model and the analytical solution is shown in Figures 3 and 4 for a 500Hz and a 8000Hz planewave source (m=0, n=0), respectively. The plotted data is extracted from the line along the center of the duct. Note that the CDUCT and the analytical solutions are identical. With flow (M=0.8), the solutions are compared in Figures 5 and 6 for a 500Hz and an 8000Hz planewave source, respectively. Once again, the solutions are identical.

The solutions for higher order source duct modes (m,n)=(1,0), (2,0), (3,0) are shown in Figures 7, 8, and 9, respectively for a no flow case and a frequency of 500Hz. The data in Figure 7 and Figure 9 is extracted from a line which is parallel to the z direction and starts at the point (x=0.25m, y=0.25m). The data in Figure 8 is extracted from the line along the center of the duct. The results for the first higher order mode (Figure 7) show very little differences. However, the results for the second higher order mode (Figure 8) show a phase error. For the third higher order mode (Figure 9), the exact solution decays exponentially while the CDUCT solution is damped but still propagates. These results can be explained by the limitations in the parabolic approximation in CDUCT [5]. The parabolic approximation is good for waves propagating at small angles to the main axis. At larger angles, the approximation has an incorrect phase velocity. At cut-off, the parabolic method will still produce a propagating wave that requires numerical damping to minimize its impact on the solution. In general, the CDUCT code gives good results for this analytical test case subject to the limitations in the parabolic approximation.

3.2 NASA Langley Grazing Flow Impedance Tube

CDUCT is validated with experimental data from the NASA Langley Grazing Flow Impedance Tube.

The NASA Langley Grazing Flow Impedance Tube is used to evaluate acoustic liner specimens in a controlled flow and acoustic environment [9]. The test section has a 50.8 X 50.8 mm cross-section with a test specimen length of 406.4mm. The Mach number can reach 0.6 and the useful frequency range is 0.3 to 3.0 kHz. The sound pressure level can reach 155dB at the test specimen leading edge. Two flush mounted microphones are used to acquire acoustic data in the test section. One microphone is located on a side wall at the leading edge of the test specimen while the other microphone is mounted on a traversing bar at the top of the test section. At each traversing microphone location, the complex acoustic pressure, sound pressure level, and phase can be determined relative to the fixed microphone. A sketch of the test section is shown in Figure 10. The facility is designed to operate below the cut-on frequency of any higher order modes. Note that high-order mode effects are unavoidable near the acoustic liner specimen.

Experimental data from a hardwall insert and a ceramic tubular liner (CT65) are used for this validation case. The speed of sound is assumed to be 340.3m/s. The frequency range is 0.5 to 3.0 kHz with 0.5kHz increments. The Mach number is assumed to be uniform throughout the duct. The test section in Figure 10 is discretized into a uniformly spaced three-dimensional grid of size 11 X 11 X 129. The initial acoustic source at z=0 is a planewave with the amplitude set to the value measured at the first traversing microphone location.

The hardwall insert provides an infinite impedance condition. This is useful in examining the baseline flow and acoustic response of the facility. In order to simulate a hardwall boundary condition in CDUCT, a specific resistance equal to 1000 and zero specific reactance are specified at the wall boundaries. For no flow (M=0.0), the sound pressure level from CDUCT is compared to the experimental data in Figure 11. The real and imaginary parts of the acoustic pressure are shown in Figure 12. The CDUCT results are very close to the experimental data. It is observed that the facility does not have a perfectly anechoic termination and therefore acoustic waves are reflected upstream. This is illustrated by the small oscillations in the sound pressure level. The CDUCT parabolic approximation does not account for these reflected waves. For a flow of M=0.3, the sound pressure level from CDUCT is compared to the experimental data in Figure 13. The real and imaginary parts of the acoustic pressure are shown in Figure 14. The CDUCT results are close to the experimental data. The main difference in the sound pressure level is the oscillations in the experimental data. These oscillations are larger than the oscillations in the no flow case. A small phase error is also observed in the real and imaginary acoustic pressure plots. The main sources of these errors are the acoustic waves that are propagating in the upstream direction and the assumption of uniform flow in the duct.

The impedance of the ceramic tubular liner (CT65) is fairly insensitive to the flow Mach number and sound pressure levels. This allows the use of a single baseline impedance for the entire flow range. This baseline impedance was obtained from a conventional normal incidence impedance tube and is listed in Table 1. For no flow (M=0.0), the sound pressure level from CDUCT and the experimental data are

Table 1. Baseline Impedance of Ceramic Tubular Liner (CT65)

Frequency	Specific Resistance	Specific Reactance
500	0.466	-1.411
1000	0.546	0.084
1500	1.449	1.168
2000	3.294	-0.455
2500	1.224	-1.145
3000	0.764	-0.154

shown in Figure 15**.** The real and imaginary parts of the acoustic pressure are shown in Figure 16. The CDUCT results have the correct trends and are close to the experimental data except at the lowest frequency (500Hz). The ceramic liner scatters the planewave mode into higher order modes. These higher order modes are cut-off, which results in phase errors in the CDUCT parabolic approximation. For a flow of M=0.3, the sound pressure level from CDUCT and the experimental data are shown in Figure 17. The real and imaginary parts of the acoustic pressure are shown in Figure 18. The CDUCT results compare favorably with the experimental data except at the lowest frequency (500Hz). The main sources of error are the higher order mode effects near the liner, acoustic waves propagating in the upstream direction, and the uniform Mach number assumption.

3.3 Rectangular Flow Duct

In the mid 1970's, Kraft et. al [10] studied two-element acoustic liners in a rectangular flow duct. CDUCT is used to model this flow duct, and the calculated power level attenuations are compared to the measured values. A schematic of the duct is shown in Figure 19. A unique feature of the experimental study was the measurement of the acoustic source pressure profile. This was accomplished with the use of a traversing microphone and a stationary microphone which obtained both the source pressure amplitude and phase information. In an attempt to design optimized two-element acoustic liners, Kraft et. al used the initial measurement of the source characteristics as input into a prediction and design code to come up with an optimized acoustic lining at a single frequency. The performance of the liner did not meet their predicted attenuation levels and it was discovered that backwards traveling waves were affecting the source modal content. This was evident since when the acoustic lining was changed, the source modal content changed as well. Note that CDUCT does not account for the backwards traveling wave and therefore the comparison of the power attenuations will not be very accurate. The trends exhibited for the different acoustic lining configurations does provide interesting information.

Five different configurations of acoustic lining are given in Table 2. The source complex pressure

Table 2. Configuration Lining Impedance

Configuration	Section 1	Section 2
1	0.90-1.4i	0.90-1.7i
2	0.64-1.15i	0.75-0.55i
3	0.75-0.55i	0.64-1.15i
4	0.43-1.3i	0.64-0.6i
5	0.75-1.2i	0.90-0.55i

profile for each lining configuration was scanned and digitized from Reference 10 for input into the CDUCT simulation. A uniform rectangular grid of size 9 X 22 X 97 in the x, y, and z directions, respectively, is used for the CDUCT simulation. The mean flow Mach number is given as 0.3. Table 3 shows the comparison of the CDUCT results with the measured power attenuations for the five configurations. In general the CDUCT results are good. It is interesting to note that the only difference

Table 3. Comparison of Power Attenuations

Configuration	Frequency (Hz)	CDUCT (dB)	Measured (dB)
1	2000	15.4	21.5
2	1950	17.5	20.0
3	1950	12.2	11.0
4	1940	18.5	16.5
5	1900	30.7	26.1

between Configuration 2 and 3 is that the positions of the liners are switched. This results in a measured decrease in attenuation for Configuration 3, which is predicted with CDUCT. The main sources of error are the uncertainty in the impedance values of the liners, the uncertainty in the acoustic source amplitude and phase, and the existence of backwards traveling waves in the experiment.

3.4 Annular Flow Duct

Syed et. al [11] studied an acoustically treated straight annular exhaust duct with a realistic fan stage as the flow and acoustic source. The number of outlet guide vanes was chosen to generate strong rotor/stator interaction tones. The modal coefficients upstream and downstream of the treated section were measured with specially designed mode probes. A schematic of the treated section is shown in Figure 20. The axisymmetric option in CDUCT is used to model the annular flow duct. A computational grid of size 21 X 117 in the R and X directions, respectively, is used for the CDUCT simulation. The impedance, frequency, and flow are given in Table 4. For the CDUCT prediction, specified spinning

Table 4. Annular Duct Experimental Parameters

Frequency (Hz)	Specific Resistance	Specific Reactance	Mach
1000	0.51	-1.82	0.21
1500	0.51	-1.00	0.32
1900	0.51	-0.55	0.40

modes and cut-on radial modes are used with an equal energy per mode assumption. The power attenuations are compared with the measured values in Table 5. The calculated attenuations match very

Table 5. Comparison of Power Attenuations for a Given Mode

Frequency (Hz)	Spinning Mode	Radial Mode	CDUCT (dB)	Measured (dB)
1000	-1	1	2.32	2.18
1500	-1	1,2	8.19	3.72
1900	-1	1,2	17.17	16.83
1900	7	1	23.71	22.59

closely to the measured values at 1000Hz and 1900Hz. However, the comparison at 1500Hz is not good. Errors from the source modal content and equal energy per mode assumption could explain the differences. Another possible source of error is the specified impedance values.

3.5 Prediction Validation Conclusions

The CDUCT code is successfully validated against both analytical and experimental results. CDUCT is accurate for duct acoustic propagation problems with acoustic treatment, flow, and different acoustic sources subject to the limitations in the CDUCT parabolic approximation method. The main limitation to the accuracy is that waves propagating at large angles with respect to the main axis have a phase error. Cut-off modes are damped numerically though they may still introduce some error to the solution. Another limitation to CDUCT is that it approximates a one-way convected Helmholtz equation and ignores backwards traveling waves.

3.0 Acoustic Lining

Noise radiation from the aft fan duct of a high bypass ratio turbofan engine accounts for a large portion of the community noise generated by commercial transport aircraft. One of the most important techniques for controlling aft fan noise is the use of acoustic lining along the walls of the duct. This acoustic lining can be described in terms of a complex impedance as a function of frequency and position along the duct wall. The CDUCT code can optimize the wall impedance to maximize the acoustic attenuation at all frequencies of interest. Note that the optimized impedance is not obtainable at all frequencies with the typical acoustic lining which is based on an array of Helmholtz resonators in a single or double layer arrangement. Nevertheless, the optimized impedance can be a useful guide in the detailed design of the acoustic lining.

4.1 Optimized Impedance

The objective is to maximize the noise power attenuation for a given frequency, duct geometry, flow, and noise source by optimizing the wall lining impedance. The aft fan duct geometry for a typical modern high bypass ratio engine is similar to Figure 21. For this analysis, the initial Mach number is assumed to be 0.4 and is allowed to vary according to the one-dimensional compressible flow Mach-area relationship. The noise source is assumed to be a planewave. In order to reduce complexity, the geometry is assumed to be axisymmetric. A computational grid of size 28 X 162 is used for the optimization calculations and is shown in Figure 22. A minimum value of 0.2 for the specific resistance is used for numerical stability. The Downhill Simplex method [12] is used to determine the optimum impedance for the uniform case (one-zone) where the inner and outer wall impedances are identical. This optimization method only requires function evaluations (no gradient information) and is easily implemented. The major drawback to this method is that it is susceptible to finding local optima since it is classified as a "hill-climbing" technique. The optimum attenuations and impedances are shown in Figures 23 and 24 and the values are listed in Table 6. Note that the impedance values are given in

Table 6. Optimized Uniform Impedance

Band	Frequency (Hz)	Attenuation (dB)	Specific Resistance	Specific Reactance
27	500	83.06	0.214	-0.338
28	630	62.63	0.364	-0.383
29	800	35.37	0.396	-0.338
30	1000	29.26	0.513	-0.452
31	1250	22.88	0.678	-0.629
32	1600	17.16	0.855	-0.902
33	2000	12.53	1.079	-1.133
34	2500	9.45	1.305	-1.116
35	3150	8.03	1.596	-1.099
36	4000	7.07	1.685	-0.806
37	5000	6.60	1.778	-0.899
38	6300	5.92	1.938	-0.942
39	8000	5.38	1.881	-0.968
40	10000	4.83	2.094	-0.992

terms of specific resistance and specific reactance, which form an ordered pair in the complex impedance plane. Since this uniform optimization case has two parameters (specific resistance and specific reactance), the attenuation contours can be plotted and are shown in Figure 25 for several frequencies. It

is observed that there exists only one optimum point for each frequency, which lends confidence that the Downhill Simplex method is sufficient. This was also observed by Dunn et. al [13] for a cylindrical duct geometry. It is also noted that at lower frequencies, the attenuation drops off rapidly as the impedance differs from the optimum impedance while at higher frequencies, the attenuation drops off slowly. Furthermore, it is observed that the attenuation contours are nearly symmetric about the optimum reactance but are asymmetric with respect to the optimum resistance. The attenuation decreases rapidly if the resistance is less than the optimum resistance. If the resistance is greater than the optimum resistance, the attenuation decreases at a slower rate.

The acoustic lining envelope is segmented into two, four, and eight-zone cases and are shown in Figure 26. For a multiple zone lining configuration, a good starting point is needed for the optimizer to be successful. Since the optimum uniform impedance distribution is a basic subset of any multiple zone lining configuration, it is chosen as the starting point for the optimizer. The optimum attenuations are shown in Figure 27 and the optimized impedances are listed in Appendix A. The optimized attenuation increases as the number of impedance zones increases. The attenuation increase for the two-zone case over the one-zone case is not large at higher frequencies. However, the improvement for the four-zone case over the two-zone case is significant over many frequencies, which suggests that there is a large potential benefit in an optimized axially segmented acoustic lining. In general, the attenuation improvement for the eight-zone case over the four-zone case is large. It is observed that the lower limit on specific resistance is reached for many frequencies in the four and eight-zone cases, which could limit the maximum obtainable attenuation. Furthermore, it is likely that locally optimum points exist for the eight-zone case. It is interesting to note that on the outer wall, the optimized impedance for a wide range of frequencies is a low resistance but reactive liner. This has been described by Hogeboom et. al [14] as a noise scattering lining since the low resistance results in a small dissipation of noise but the reactive portion of the impedance can still interact with the noise. This interaction can change the modal structure of the noise to result in more effective downstream lining. Note that it is unlikely that a passive acoustic liner can be manufactured that achieves the optimized multi-zone impedances over a wide range of frequencies.

4.2 Lining Design

The objective of the acoustic lining design is to obtain sufficient noise attenuation over a frequency range that is important for the overall aircraft noise signature. The lining design must account for many constraints such as maximum lining depth, maximum lining area, structural strength, cost, and maintenance requirements. These constraints often limit the amount of noise attenuation that can be achieved. Furthermore, it is noted that the optimized impedances are not physically obtainable for a wide range of frequencies at the same time with the typical acoustic lining design.

An example aft fan duct is shown in Figure 28 where the acoustic lining areas are labeled. It is observed that the example lining can be considered to have four zones. The typical Boeing acoustic liner consists of a double layer liner with a perforated facesheet and a buried septum. The parameters to be specified by the lining design are the percent open area of the facesheet and septum, and the two cavity depths. A Boeing proprietary acoustic lining model was coupled to the CDUCT code in such a way that the lining parameters are evaluated which results in impedance which is then evaluated to result in attenuation. This process is repeated for all frequencies of interest.

The CDUCT code requires that the noise source be specified in terms of acoustic potential at the inlet of the duct. Since this data is seldom known, a noise source must be assumed for the lining design process. For the geometry discussed in Section 4.1 (Figure 21), a 5kHz noise source which is described

by a gaussian distribution was evaluated at different radial positions in the duct with a wall impedance of 1.0-1.0i. The results for three different source widths are shown in Figure 29. It is observed that for a source near the outer wall of the duct, the attenuation is at a minimum. The flow and geometry of the duct allow a source near the outer wall to have fewer interactions with the acoustic lining. Essentially, using a line-of-sight argument, the noise beams directly out of the duct. This tip noise source which represents a least attenuated source is used in the example lining designs. It is interesting to note that in a fan rig study, Morin [15] shows that broadband noise from a rotor/stator interaction is typically dominated by a noise source from the tip region.

The tone corrected perceived noise level (PNLT) metric is used to evaluate the lining design. The effective perceived noise level (EPNL) metric is not used since the CDUCT code in its present form only predicts in-duct power attenuations and does not accurately describe the noise radiated to the farfield from the aft fan duct. Experience shows that at the maximum PNLT angle (typically 120° or 130°) the attenuation provided from in-duct power attenuations are applicable and the PNLT attenuation gives a good estimate of the overall lining benefit.

For the example aft fan duct in Figure 28, a computational grid of size 28 X 162 was generated. To reduce complexity, the axisymmetric case is analyzed. The initial Mach number is 0.463. A gaussian tip source shown in Figure 30 is used for the analysis. Figure 31 shows the hardwall and baseline treated aft fan spectra at the maximum PNLT angle for a typical narrow-chord turbofan engine. The CDUCT code was used to evaluate the baseline lining, which results in the attenuation shown in Figure 32. The attenuation calculated with the gaussian tip source does not perfectly match the attenuation calculated from the difference between the measured hardwall and treated spectra. This indicates that the assumed gaussian tip source does not describe the true noise source. However, the gaussian tip source is intended to represent a least attenuated source that should be applicable in designing the acoustic lining. In order to evaluate the various lining designs which were designed using the gaussian tip source, differences in attenuations relative to the calculated baseline attenuation (Figure 32) are applied to the baseline treated spectrum (Figure 31). A six- zone lining is created by dividing the inner wall of the example aft fan duct into three sections and by keeping the three outer wall sections the same. The double layer lining parameters were allowed to vary to optimize the attenuation at the blade passage frequency (BPF), Band 33, while maintaining a certain level of attenuation at higher frequencies. Figure 33 shows the attenuation spectrum for the six-zone lining where the baseline attenuation is shown for reference. Note that at the BPF and 2BPF, the optimized attenuation is greater than that from the baseline lining. At higher frequencies, the attenuation is very close to the baseline. The resulting PNLT benefit relative to the baseline is a 33.7% increase in attenuation. The acoustic pressure contours and axial acoustic intensity for a frequency of 2kHz are shown in Figure 34(a,b,c,d) for the baseline and six-zone designs. It is observed that the six-zone design scatters a large portion of the noise into the inner wall, while the other portion remains close to the outer wall. Essentially, the noise is conditioned such that it is more effectively absorbed by the downstream acoustic lining. This differs from the conventional lining design philosophy of maximizing the attenuation of the noise in each lining segment. Furthermore, the inner wall of the six-zone design has very little reflection while the baseline design reflects a portion of the noise.

A highly curved geometry is shown in Figure 35. For this geometry, if flow convection effects are ignored, a tip noise source will not have a direct line-of-sight to the duct exit. The baseline lining is evaluated for this geometry where the effective lining length-to-height ratio is set equal to that for the conventional geometry. The attenuation spectrum is shown in Figure 36 where the predicted attenuation from the baseline conventional geometry is included for reference. With equivalent linings and noise sources, the highly curved geometry results in more attenuation at higher frequencies compared to the

conventional geometry. It is noted that the initial and final Mach numbers are the same for the two geometries, but the Mach number throughout the ducts are different. The PNLT benefit for the highly curved duct is 7.9%. For a six-zone lining design, the attenuation spectrum is shown in Figure 37 where the attenuation from the baseline conventional geometry is shown for reference. The attenuation at BPF is much greater for the six-zone design in the highly curved geometry than for the baseline lining in the conventional geometry. The attenuations at higher frequencies are also greater for the highly curved geometry. The PNLT benefit for the six-zone design is 69.2% and all of the attenuation results are summarized in Table 7. The acoustic pressure contours and axial acoustic intensity for a frequency of 2kHz is shown in

Table 7. Summary of PNLT Attenuation Results

Configuration	PNLT (dB)	ΔPNLT (dB)	% Benefit re. Baseline
Hardwall Conventional Duct	102.10	NA	NA
Baseline Treated Conventional Duct	94.14	7.96	NA
6-Zone Optimized Conventional Duct	91.46	10.64	33.7%
Baseline Treated Highly Curved Duct	93.51	8.59	7.9%
6-Zone Optimized Highly Curved Duct	88.63	13.47	69.2%

Figure 38(a,b,c,d) for the highly curved geometry with baseline and six-zone designs. The source scattering effect for the six- zone design is observed. The noise incidence angle on the inner wall lining near the hump is large due to the high curvature which allows the lining to absorb a large portion of the noise when the lining parameters in that section are designed correctly. It is noted that while the potential noise benefits are large for a highly curved geometry, the flow losses could be prohibitive.

4.3 Acoustic Lining Conclusions

The CDUCT code is capable of optimizing the wall lining impedances in the aft fan duct of a turbofan engine. Calculations indicate that there is a large potential increase in noise attenuation for an axially segmented lining; however, the optimized impedances are not obtainable by current passive lining designs for the entire important frequency range. Compromises must be made in designing the acoustic lining parameters such that constraints are met and good but not necessarily optimum attenuations are obtained in the important frequency range. For a narrow-chord aft fan spectrum in a conventional geometry, a six-zone lining was designed which produced a significant increase in PNLT attenuation. This design had a large increase in attenuation at BPF while slightly degrading the attenuation at higher frequencies. A highly curved geometry was also analyzed. An attenuation benefit occurred at frequencies higher than BPF for the baseline lining design. For a six-zone lining design, the highly curved geometry produced a large increase in BPF attenuation without degrading the attenuations at higher frequencies. The highly curved geometry produced a significant increase in PNLT attenuation; however, the flow losses could be prohibitive. The six-zone designs for both conventional and highly curved geometries utilized noise scattering lining that enabled the downstream lining to be more effective.

4.0 ICD Array Mode Measurement

A unique application for the CDUCT code is the inflow control device (ICD) microphone array. An ICD is typically used during static noise testing of model fan rigs or full scale turbofan engines. Its purpose is to prevent large-scale turbulence and ground vortices from being ingested into the engine and interacting with the rotor, which causes extraneous tone noise. A typical ICD has a spherical-like shape with a large honeycomb cell structure that is acoustically transparent. The microphone array is used to measure the amplitude and phase of the engine noise signature at known locations on the ICD structure. The CDUCT code is used to propagate a series of cut-on acoustic modes from a location in the inlet to the ICD microphone array to form a set of basis functions. Once the CDUCT basis functions are calculated, the microphone array data can be processed to determine the acoustic modal structure of the fan noise. This concept was tested in the NASA Glenn Active Noise Control Fan (ANCF) Facility.

5.1 NASA Glenn Active Noise Control Fan

The ANCF consists of a low speed, large diameter, ducted fan that is used to investigate both active noise control concepts and general fan aeroacoustics [16,17]. A schematic of the facility is shown in Figure 39. The inlet duct has a constant four-foot diameter and surrounds a rotor consisting of 16 composite blades. Two unique features include an externally supported duct such that the rotor noise can be evaluated without interactions from vanes or struts and the rotating rake mode measurement system. This mode measurement system characterizes the modal structure at the BPF and harmonics, and details of its operation can be found in References 16 and 17. The ICD array results can be directly compared with the rotating rake results.

5.2 ICD Microphone Array and Data Processing

The ICD microphone array used 40 Knowles cylindrical type microphones arranged in 4 rings with 10 non-uniformly spaced microphones in each ring. The locations are listed in Appendix B. The microphone data is synchronized with the shaft angular position. The CDUCT code is used to predict the complex acoustic pressures at the microphone locations for each cut-on acoustic mode. A computational grid of size 35 X 61 X 169 (radial, circumferential, axial) is used for the BPF calculations (Figure 40) and a grid of size 40 X 61 X 169 is used for the 2BPF calculations. Note that the CDUCT code must have both inner and outer wall boundaries due to the code's treatment of boundary conditions, which results in a three-inch fake centerbody. A hardwall extension is used to connect the inlet to the ICD. The specific resistance of the inner and outer walls is set equal to 1000 and the specific reactance is set to zero in order to simulate the hardwall boundary condition. An example CDUCT solution for the (-4,0) mode at 2BPF is shown in Figure 41. The complex acoustic pressure at the microphone locations is interpolated from the solution at the grid points. The synchronized microphone data is processed by first taking many averages over the shaft angular position and then taking the Fourier transform of the averaged data to obtain the complex acoustic pressure at BPF and 2BPF for each microphone. Due to the $e^{-i\omega t}$ dependence in CDUCT, the negative frequencies are used in the Fourier transform analysis.

The complex acoustic pressures from the CDUCT solutions can be written as a matrix, Q, whose rows indicate the acoustic mode and the columns indicate microphone number. The analyzed data from the microphones can be written as a vector, G. In a beamforming operation

$$BF = Q^{*}G \tag{41}$$

where BF is a vector and represents the estimate of power for each mode.

5.3 Comparison of Test Results

For the current test, 30 stators were used along with 10 or 15 uniformly spaced cylindrical rods, which were placed in front of the 16-blade rotor. The cylindrical rods generate a periodic disturbance that interacts with the rotor to generate spinning modes. Another source for spinning modes is the rotor/stator interaction. The paper by Tyler and Sofrin [18] describes the theory of spinning mode generation from periodic disturbances relative to the rotor. The governing equation is

$$m = nB \pm kV \qquad k = 0,1,2,... \tag{42}$$

where m is the spinning mode order, n is the harmonic index, B is the number of rotor blades, k is an integer, and V is the number of stators or rods. At a corrected shaft speed of 2200 RPM, the expected spinning and radial modes are listed in Table 8. The Mach number in the duct is given as 0.09. Note that

Table 8. Expected Modes in ANCF at 2200 CRPM

Configuration	BPF	2BPF
10 rods, 30 stators	(-4,0)	(2,0), (2,1), (2,2), (2,3), (-8,0)
15 rods, 30 stators	(1,0)	(2,0), (2,1), (2,2), (2,3)

the listed expected modes are limited to only cut-on modes. Figures 42 and 43 show the comparisons between the ICD array and the rotating rake for BPF and 2BPF, respectively, for the 10-rod configuration at 2200 CRPM. Figures 44 and 45 show the comparisons for BPF and 2BPF, respectively, for the 15-rod configuration. It is observed that the ICD array finds the expected modes listed in Table 8 and matches the rotating rake results. The rotating rake measurement has a much better signal-to-noise ratio (SNR) than the ICD array. Some improvement in SNR can be obtained with additional microphones in the ICD array. Several factors affect the accuracy of the ICD array such as the overall layout of the microphones, the CDUCT propagation accuracy, the accuracy of the microphone position information, and the microphone phase accuracy. The calculated radial modes do not match well. In order to improve the radial mode separation, the radius of the fake centerbody could be decreased or the microphone array design could be improved to better resolve the radial modes. One advantage with the ICD array over the rotating rake is the possibility of resolving the acoustic modes for broadband noise. Another advantage is that the ICD array is less intrusive. In general, the ICD array performs well in characterizing the acoustic modal structure of the NASA Glenn ANCF.

5.0 Conclusions and Recommendations

The CDUCT parabolic approximation can efficiently model the acoustic propagation in an aft fan duct. The code can account for three-dimensional effects, lining, and flow. The solution method has been validated with both analytical solutions and experimental data to establish its accuracy and explore its strengths and limitations. Studies of wall lining impedance optimization indicate a large potential benefit for an axially segmented lining. The optimum impedance studies also indicate the importance of a noise scattering lining segment that increases the effectiveness of the downstream lining. It is noted that the optimized impedance can not be obtained at all frequencies with a current passive acoustic lining. A six-zone acoustic lining was designed for a typical turbofan engine geometry with a narrow-chord fan spectrum that produced a significant increase in PNLT attenuation. A highly curved geometry aft fan duct was also studied which resulted in significant increases in PNLT attenuation for a baseline and six-zone lining design. The highly curved geometry has a greater potential for noise attenuation than a conventional geometry because of a line-of-sight argument and the potential for a larger wave incidence angle on the wall lining. It is noted that the flow losses due to the highly curved geometry could be prohibitive. In an interesting application for the CDUCT code, an ICD mode measurement system was tested and validated against the rotating rake mode measurement system at the NASA Glenn ANCF.

It is recommended that the CDUCT lining designs be experimentally validated. The noise scattering lining must be examined further in order to exploit its capabilities. A very important assumption is made for the noise source used for the various lining designs. While there is reasonable evidence that a noise source near the outer wall can be used to design the acoustic lining, more noise source studies must be made both analytically and experimentally to characterize the fan noise. While the circumferential distribution of fan noise has been studied, more emphasis is needed to characterize the source in the radial direction for both tone and broadband noise. It is recommended that more code validation studies be performed on model scale or full-scale turbofan engines and other experimental facilities. It would be interesting to directly compare CDUCT results with finite element or computational aeroacoustics codes. Improvements to the code such as better flow modeling, boundary layer effects, a wider angle parabolic approximation, farfield radiation, or modeling the effect of reflections should be explored. The ability to analyze different geometries such as one with a fan duct splitter should also be added. Finally, the ICD mode measurement system and similar phased arrays that utilize the CDUCT acoustic duct propagation capabilities should be investigated further, especially in regards to broadband noise.

Appendix A Optimum Specific Impedances for 2, 4, and 8-Zone Cases

Two-Zone

Frequency (Hz)	R1	X1	R2	X2
500	0.213	-0.332	0.216	-0.345
630	0.295	-0.410	0.441	-0.338
800	0.383	-0.198	0.471	-0.576
1000	0.527	-0.322	0.510	-0.701
1250	0.721	-0.533	0.590	-0.827
1600	0.916	-0.894	0.732	-0.943
2000	1.181	-1.168	0.886	-1.051
2500	1.577	-0.923	0.586	-1.255
3150	1.851	-0.866	0.443	-1.443
4000	1.916	-0.575	0.200	-1.212
5000	2.077	-0.551	0.200	-1.335
6300	2.163	-0.531	0.202	-1.480
8000	2.153	-0.567	0.237	-1.706
10000	2.254	-0.572	0.277	-1.936

4-Zone

Frequency (Hz)	R1	X1	R2	X2	R3	X3	R4	X4
500	0.211	-0.402	0.255	-0.239	0.200	-0.401	0.258	-0.287
630	0.299	-0.409	0.289	-0.367	0.471	-0.313	0.410	-0.328
800	0.481	-0.499	0.243	-0.192	0.525	-0.658	0.333	-0.280
1000	0.547	-0.753	0.285	-0.162	0.451	-0.918	0.413	-0.220
1250	0.575	-1.061	0.202	-0.095	0.200	-1.095	0.397	-0.180
1600	1.288	-2.212	0.345	-0.467	0.200	-0.946	0.442	-0.049
2000	1.006	-3.068	0.427	-0.529	0.200	-1.088	0.606	-0.111
2500	1.450	-4.845	0.547	-0.639	0.200	-1.238	0.754	-0.044
3150	9.880	-9.271	0.667	-0.812	0.200	-1.398	0.799	-0.046
4000	1.736	6.795	0.705	-1.073	0.200	-1.608	0.763	0.004
5000	2.768	2.288	0.983	-1.273	0.200	-1.830	0.899	-0.333
6300	3.140	0.948	1.321	-1.333	0.200	-2.139	1.281	-0.826
8000	2.264	0.472	1.518	-1.509	0.200	-2.243	1.942	-1.132
10000	2.323	0.387	1.586	-1.704	0.200	-2.576	2.010	-0.906

8-Zone

Frequency (Hz)	R1	X1	R2	X2	R3	X3	R4	X4
500	0.211	-0.402	0.211	-0.402	0.255	-0.239	0.255	-0.239
630	0.297	-0.506	0.298	-0.344	0.241	-0.407	0.304	-0.270
800	0.513	-0.473	0.476	-0.515	0.245	-0.204	0.245	-0.119
1000	0.506	-0.780	0.614	-0.733	0.262	-0.166	0.248	-0.202
1250	0.635	-1.061	0.622	-1.025	0.215	-0.178	0.216	-0.064
1600	0.461	-1.871	0.879	-1.415	0.282	-0.370	0.201	-0.087
2000	0.227	-1.838	5.271	-2.410	0.437	-0.630	0.298	-0.099
2500	10.000	-7.435	0.200	-3.143	0.438	-0.490	0.415	-0.023
3150	9.999	-1.126	9.935	2.222	0.641	-1.034	0.586	-0.395
4000	0.236	2.962	3.784	9.091	0.833	-1.280	0.384	-0.679
5000	0.373	0.075	6.169	6.982	1.168	-1.879	0.436	-0.765
6300	0.206	-1.090	0.239	9.958	1.191	-2.501	0.469	-0.864
8000	0.215	-1.579	7.517	2.823	1.257	-2.866	0.577	-0.995
10000	1.430	-3.524	0.277	2.114	0.554	-3.040	0.633	-1.101

Frequency (Hz)	R5	X5	R6	X6	R7	X7	R8	X8
500	0.200	-0.401	0.200	-0.401	0.258	-0.287	0.258	-0.287
630	0.353	-0.447	0.542	-0.299	0.416	-0.280	0.320	-0.131
800	0.532	-0.654	0.541	-0.688	0.300	-0.293	0.370	-0.259
1000	0.437	-0.948	0.422	-0.923	0.380	-0.206	0.368	-0.188
1250	0.202	-1.095	0.203	-1.095	0.416	-0.209	0.378	-0.140
1600	0.218	-0.916	0.674	-1.317	0.854	-0.022	0.356	-0.161
2000	0.788	-0.782	0.249	-1.534	2.657	1.654	0.322	-0.280
2500	0.200	-0.880	1.278	-3.907	9.198	-0.933	0.537	-0.324
3150	0.200	-1.353	0.200	-1.789	9.170	-8.151	0.588	-0.523
4000	0.200	-1.262	0.200	-3.314	1.448	-1.557	0.830	-0.090
5000	0.200	-1.333	0.204	-4.538	0.960	-1.596	1.068	-0.085
6300	0.200	-1.413	9.936	-9.767	9.979	3.919	0.748	-0.068
8000	0.200	-1.721	5.389	-2.100	1.812	-0.625	0.757	0.015
10000	0.200	-2.035	2.368	-1.313	3.641	0.841	0.847	0.019

Appendix B NASA Glenn ICD Array Microphone Locations

microphone	x (in)	y (in)	z (in)
1	-16.63	-42.70	-0.36
2	-16.63	-42.27	5.72
3	-16.63	-35.92	22.73
4	-16.63	-23.09	35.56
5	-16.63	12.03	40.61
6	-16.63	42.70	-0.36
7	-16.63	12.03	-41.33
8	-16.63	-23.09	-36.28
9	-16.63	-35.92	-23.44
10	-16.63	-42.27	-6.44
11	-30.78	-38.90	-0.61
12	-30.78	-37.32	10.35
13	-30.78	-32.72	20.42
14	-30.78	-16.16	34.78
15	-30.78	16.16	34.78
16	-30.78	38.90	-0.61
17	-30.78	16.16	-35.99
18	-30.78	-16.16	-35.99
19	-30.78	-32.72	-21.64
20	-30.78	-37.32	-11.57
21	-41.98	-30.20	-0.81
22	-41.98	-28.98	7.70
23	-41.98	-22.82	18.97
24	-41.98	-8.51	28.17
25	-41.98	12.55	26.66
26	-41.98	30.20	-0.81
27	-41.98	12.55	-28.28
28	-41.98	-8.51	-29.78
29	-41.98	-22.82	-20.58
30	-41.98	-28.98	-9.32
31	-49.03	-18.70	-0.93
32	-49.03	-17.94	4.34
33	-49.03	-12.25	13.20
34	-49.03	-2.66	17.58
35	-49.03	10.11	14.80
36	-49.03	18.70	-0.93
37	-49.03	10.11	-16.66
38	-49.03	-2.66	-19.44
39	-49.03	-12.25	-15.06
40	-49.03	-17.94	-6.20

References

1. Rice, E. J., “Attenuation of Sound in Soft Walled Circular Ducts,” NASA TM X-52442, 1968.

2. Eversman, W. and Roy, I. D., “Ducted Fan Acoustic Radiation Including the Effects of Nonuniform Mean Flow and Acoustic Treatment,” AIAA 93-4424, 1993.

3. Ozyoruk, Y., Ahuja, V., Long, L. N., “Time Domain Simulations of Radiation from Ducted Fans with Liners,” AIAA 2001-2171, 2001.

4. Dougherty, R. P., “Nacelle Acoustic Design by Ray Tracing in Three Dimensions,” AIAA 96-1773, 1996.

5. Dougherty, R. P., “A Wave-Splitting Technique for Nacelle Acoustic Propagation,” AIAA 97-1652, 1997.

6. Dougherty, R. P., “A Parabolic Approximation for Flow Effects on Sound Propagation in Nonuniform, Softwall, Ducts,” AIAA 99-1822, 1999.

7. Pierce, A. D., Acoustics: An Introduction to Its Physical Principles and Applications, Acoustical Society of America, New York, 1989.

8. Eversman, W., “Energy Flow Criteria for Acoustic Propagation in Ducts with Flow,” J. Acoust. Soc. Am., Vol. 49, No. 6, Part 1, pp. 1717-1721, 1971.

9. Watson, W. R., Jones, M. G., and Parrott, T. L., “Validation of an Impedance Eduction Method in Flow,” AIAA 98-2279, 1998.

10. Kraft, R. E., and Motsinger, R. E., “Practical Considerations for the Design of Two-Element Duct Liner Noise Suppressors,” AIAA 76-517, 1976.

11. Syed, A. A., Motsinger, R. E., Fiske, G. H., Joshi, M. C., and Kraft, R. E., “Turbofan Aft Duct Suppressor Study,” NASA CR 175067, July, 1983.

12. Press, W. H., Teukkolsky, S. A., Vetterling, W. T., and Flannery, B. P., Numerical Recipes in Fortran: The Art of Scientific Computing, 2nd Edition, Cambridge University Press, 1992.

13. Dunn, M. H., and Farassat F., “Liner Optimization Studies Using the Ducted Fan Noise Prediction Code TBIEM3D,” AIAA 98-2310, 1998.

14. Hogeboom, W. H., and Bielak, G. W., “Aircraft Engine Acoustic Liner,” U.S. Patent 5,782,082, July, 1998.

15. Morin, B. L., “Broadband Fan Noise Prediction System for Gas Turbine Engines,” AIAA 99-1889, 1999.

16. Heidelberg, L. J., Hall, D. G., Bridges, J. E., and Nallasamy, M., “A Unique Ducted Fan Test Bed for Active Noise Control and Aeroacoustics Research,” AIAA 96-1740 or NASA TM 107214, 1996.

17. Sutliff, D. L., Nallasamy, M., Heidelberg, L. J., and Elliot, D. M., “Baseline Acoustic Levels of the NASA Active Noise Control Fan Rig,” AIAA 96-1745 or NASA TM 107214, 1996.

18. Tyler, J. M., and Sofrin, T. G., “Axial Flow Compressor Noise Studies,” SAE Trans., Vol. 70, pp. 309-332, 1962.

Figures

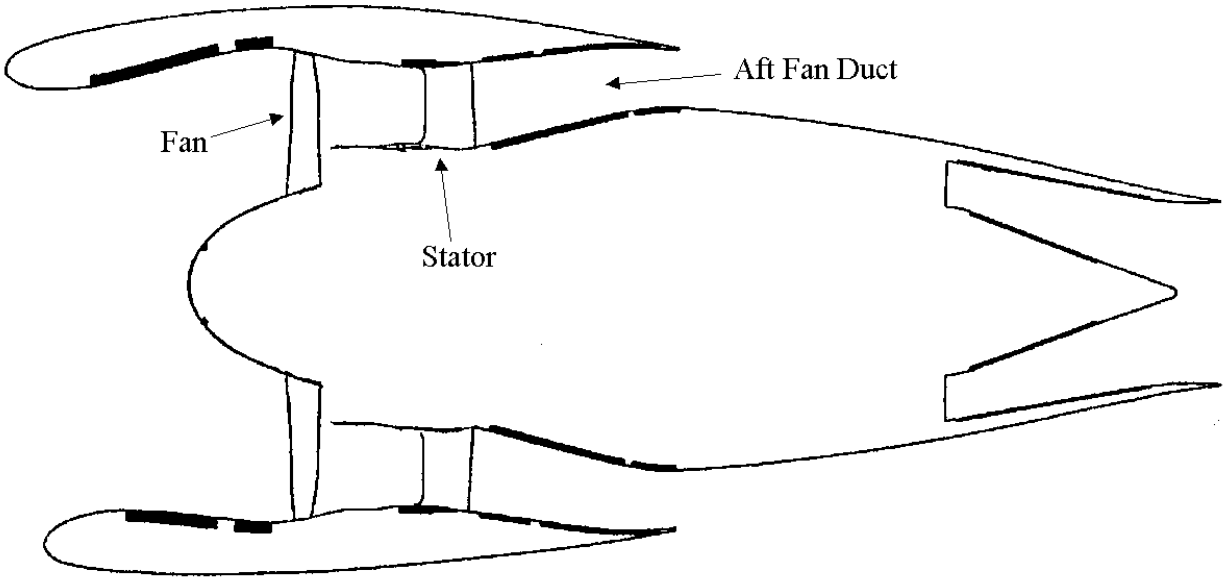

Figure 1. Typical turbofan engine geometry.

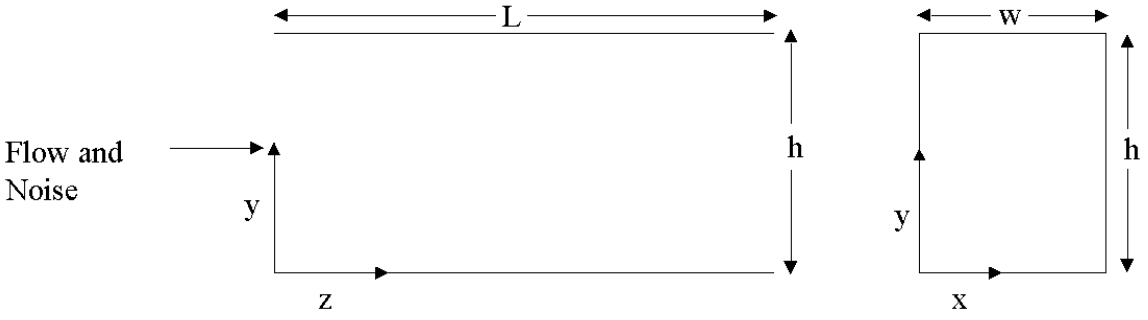

Figure 2. Rectangular hardwall duct geometry.

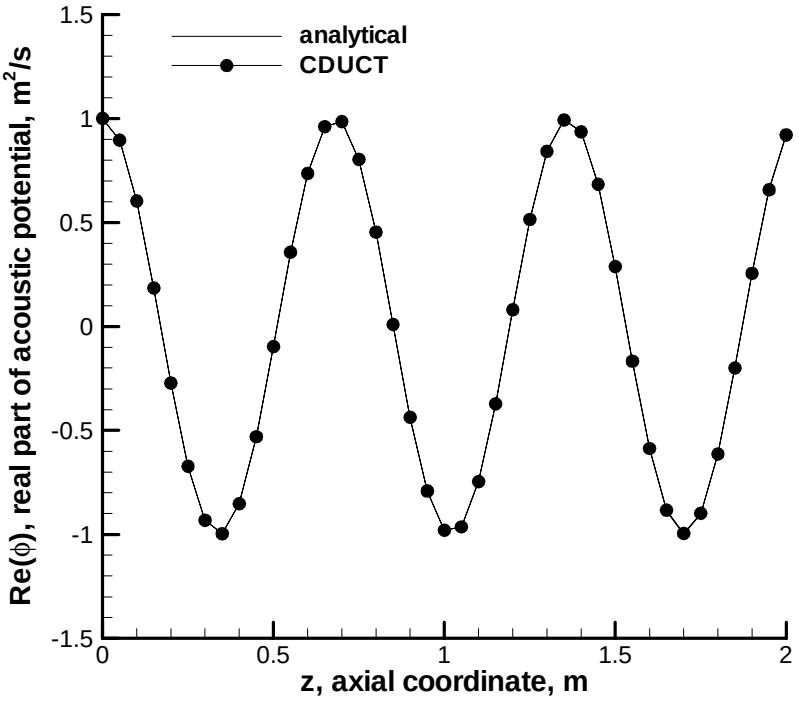

Figure 3. Comparison between CDUCT and analytical results, 500Hz, M=0.0, planewave.

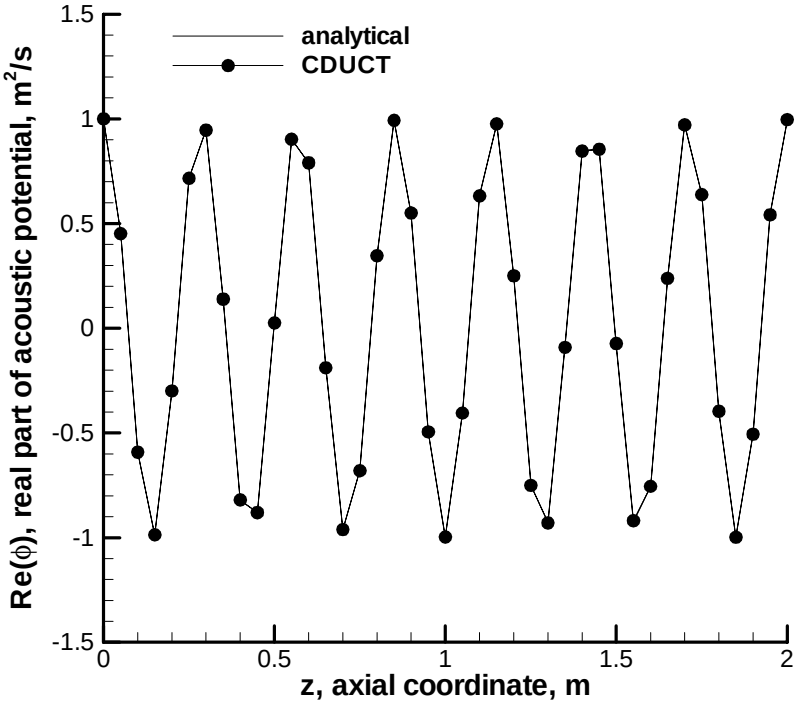

Figure 4. Comparison between CDUCT and analytical results, 8000Hz, M=0.0, planewave.

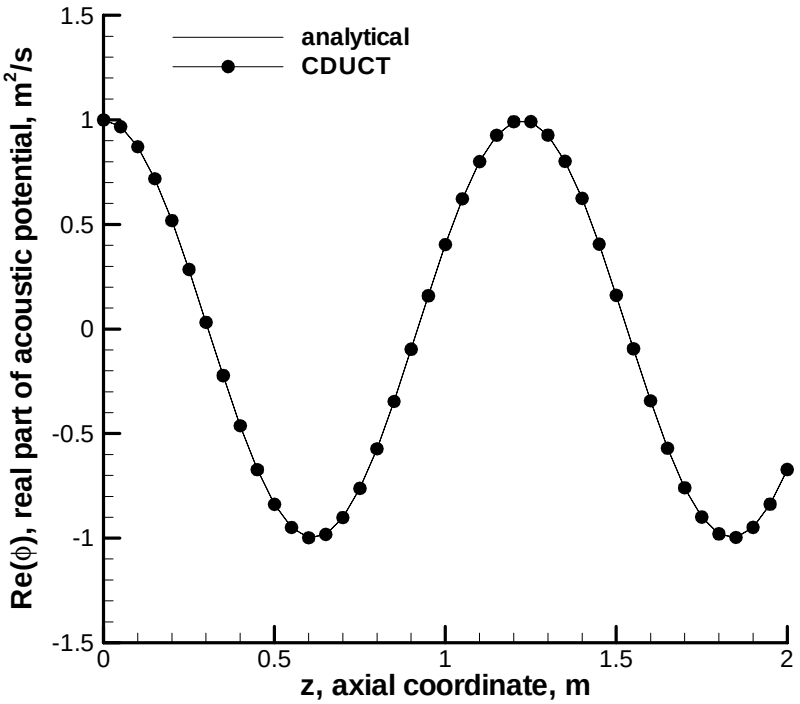

Figure 5. Comparison between CDUCT and analytical results, 500Hz, M=0.8, planewave.

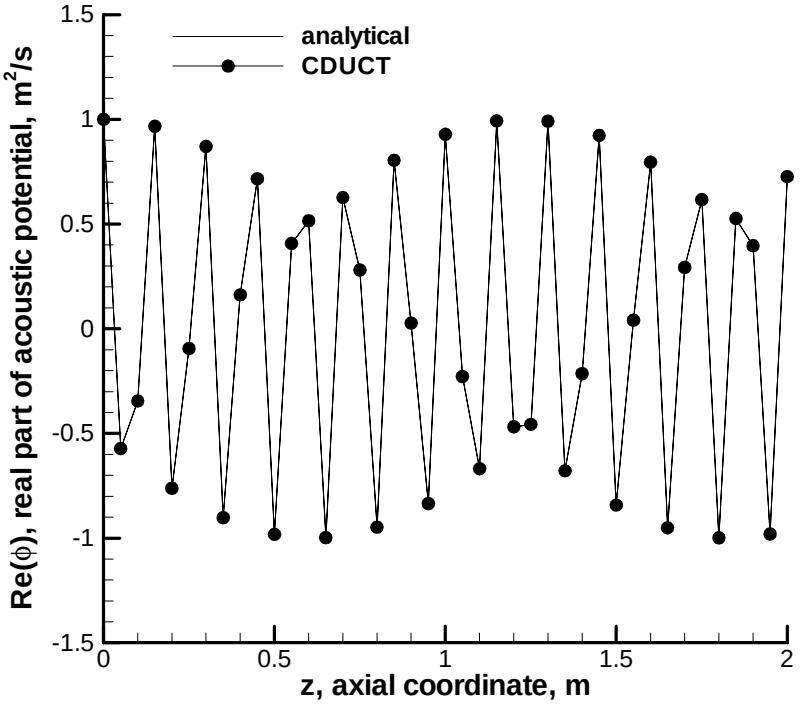

Figure 6. Comparison between CDUCT and analytical results, 8000Hz, M=0.8, planewave.

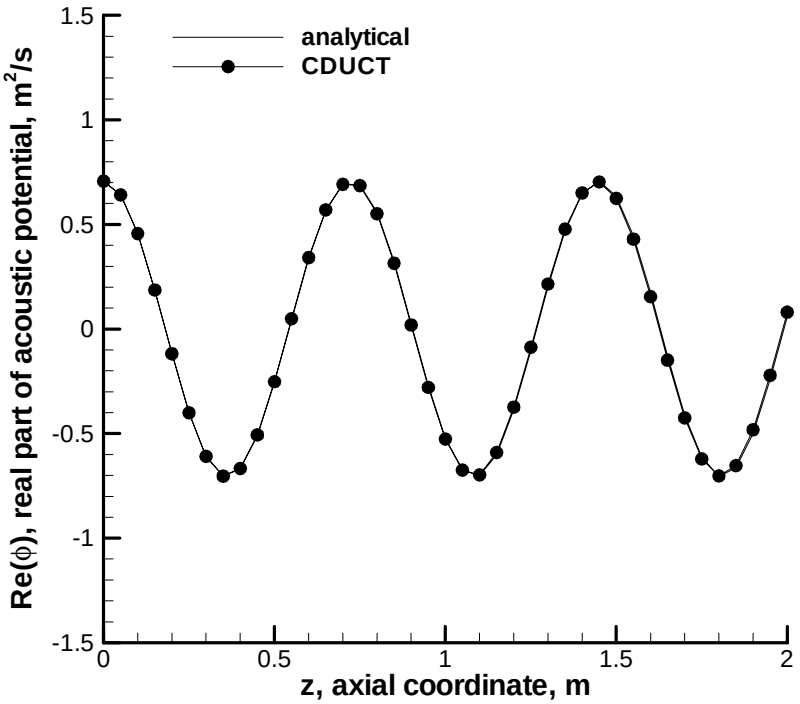

Figure 7. Comparison between CDUCT and analytical results, 500Hz, M=0.0, (1,0) mode.

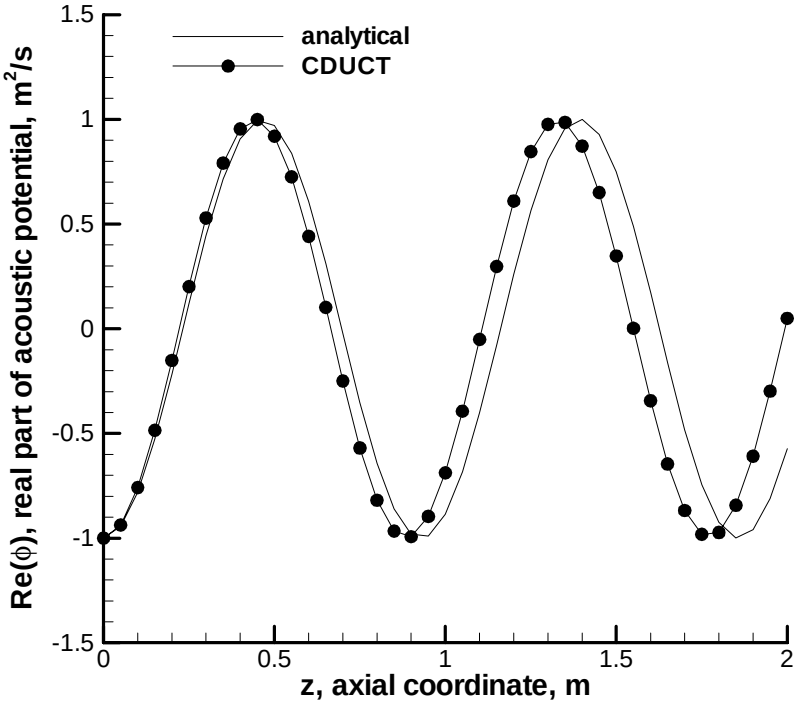

Figure 8. Comparison between CDUCT and analytical results, 500Hz, M=0.0, (2,0) mode.

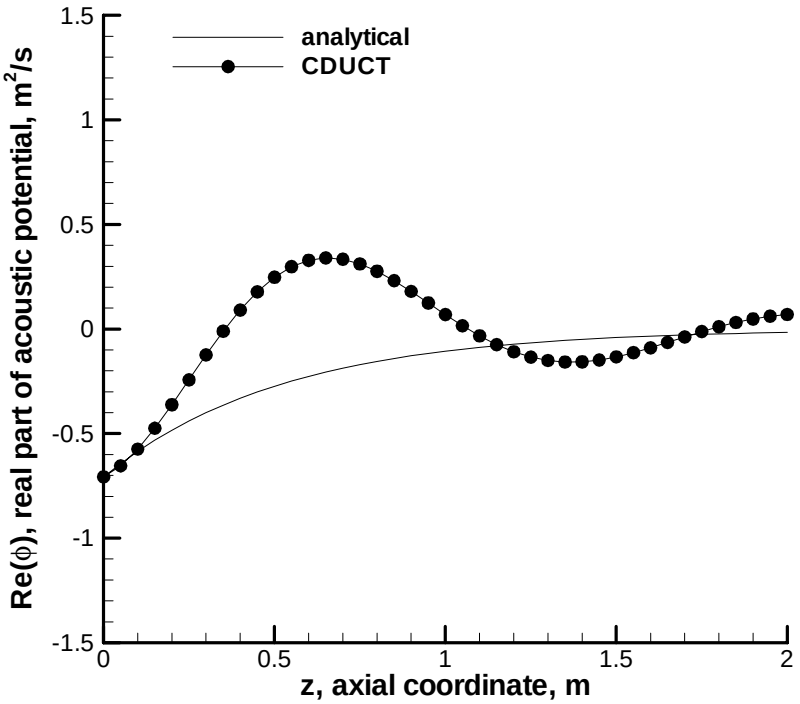

Figure 9. Comparison between CDUCT and analytical results, 500Hz, M=0.0, (3,0) mode.

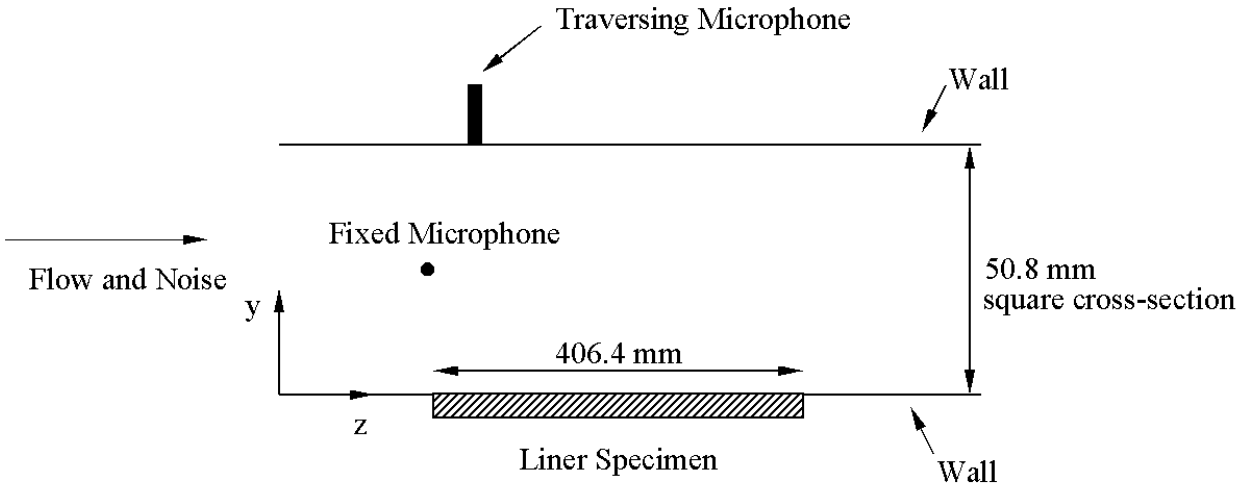

Figure 10. NASA Langley grazing flow impedance tube schematic.

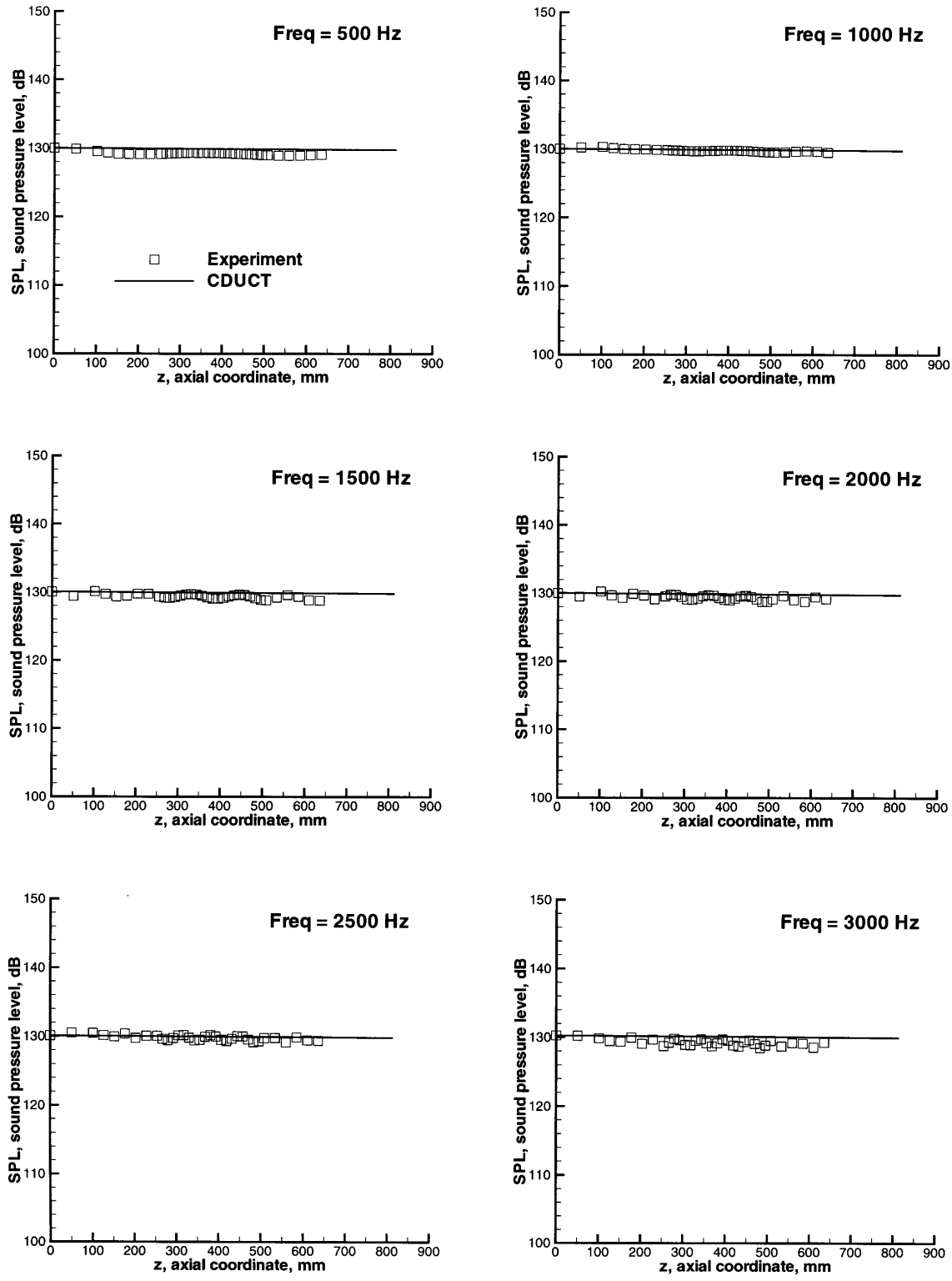

Figure 11. Hardwall sound pressure level, M=0.0.

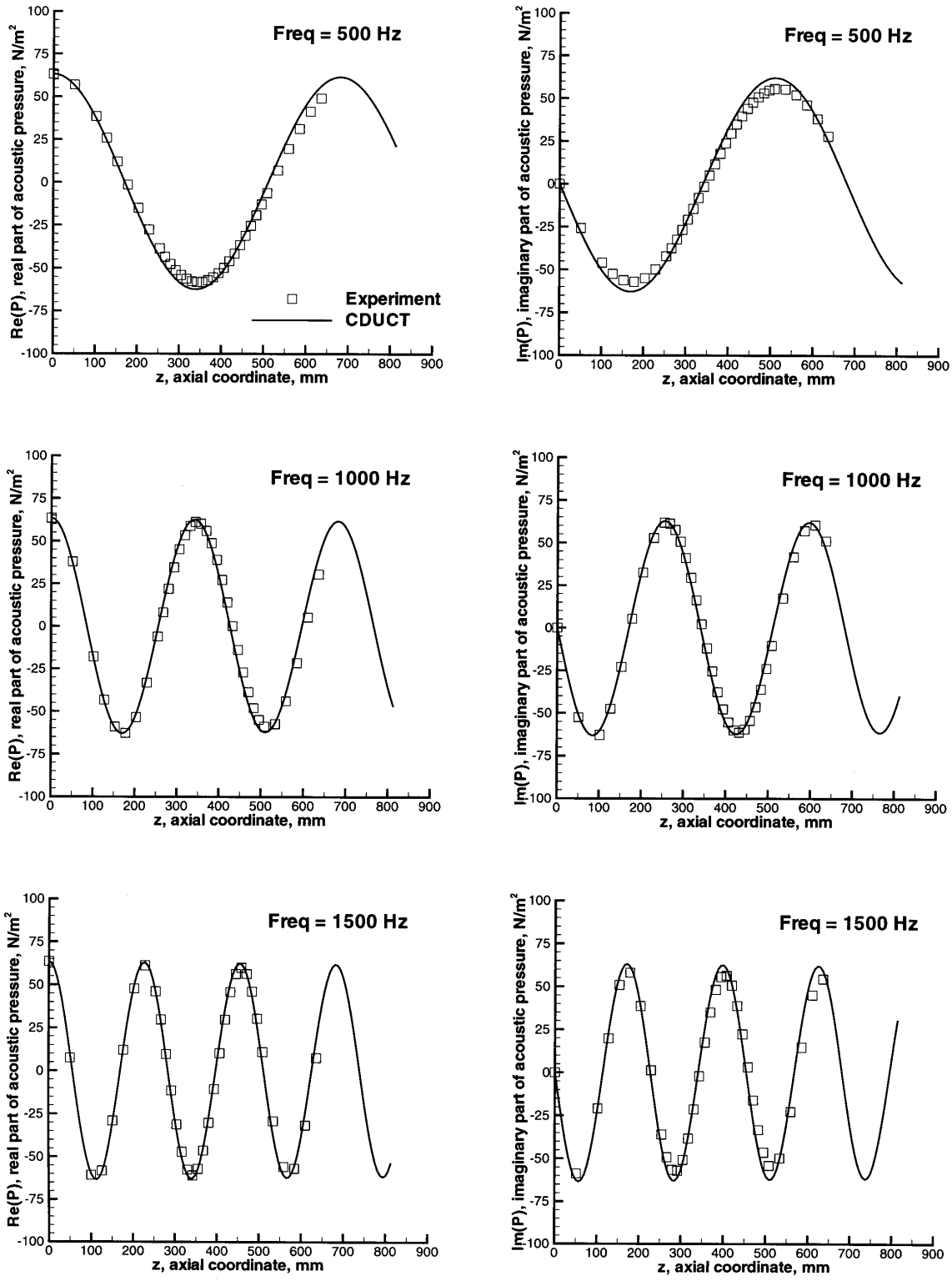

Figure 12. Hardwall real and imaginary parts of acoustic pressure, M=0.0.

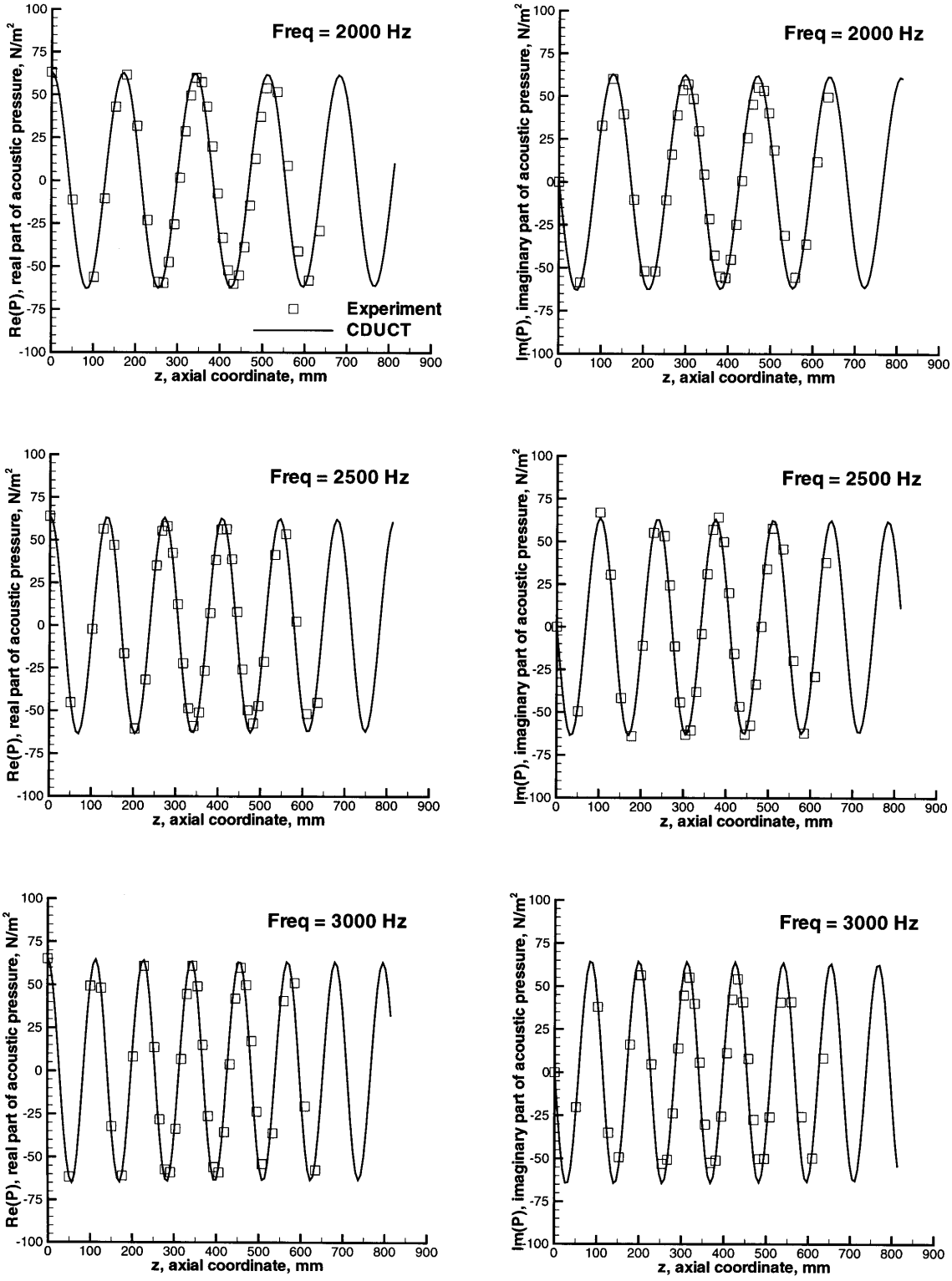

Figure 12. Concluded.

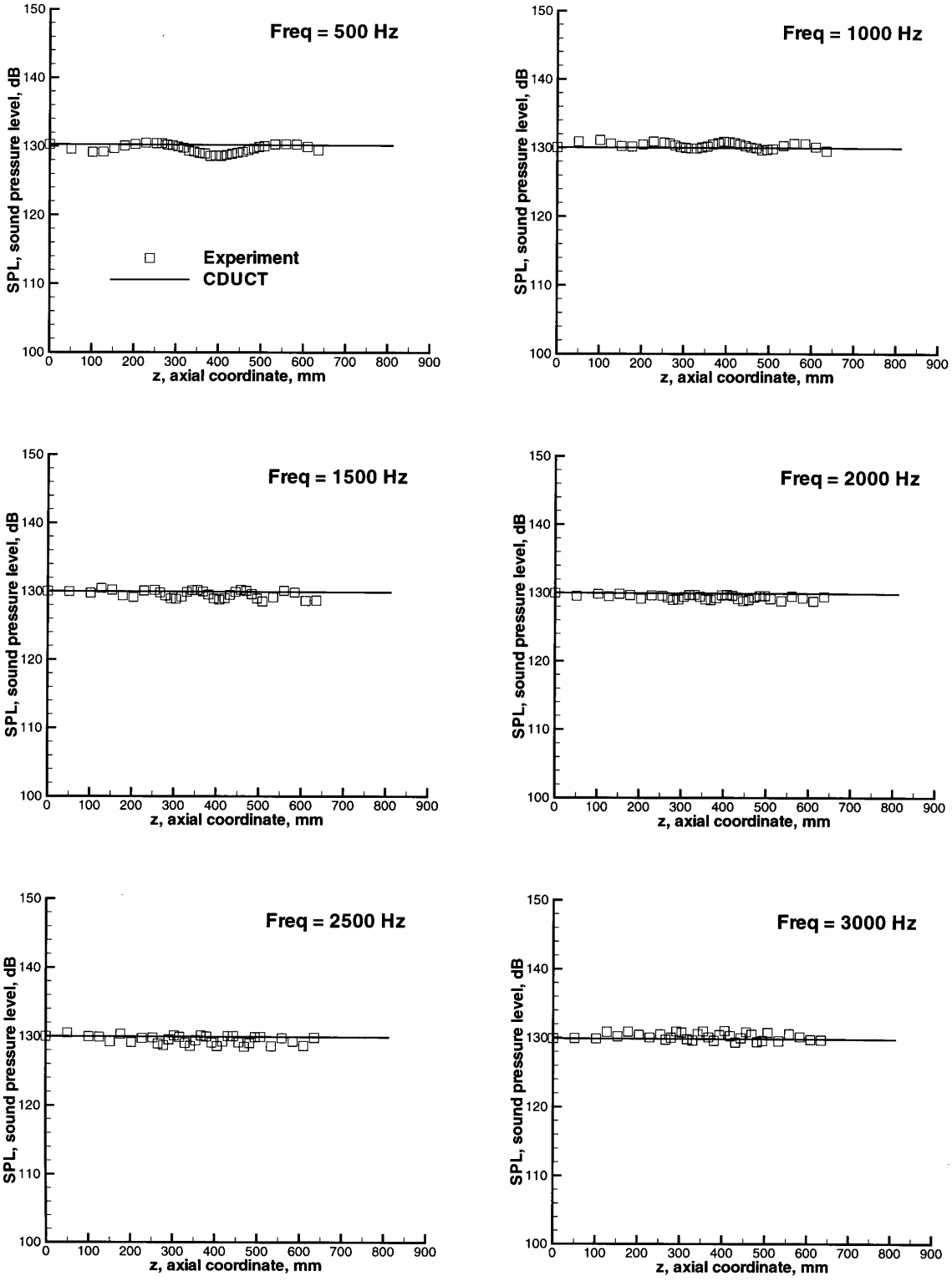

Figure 13. Hardwall sound pressure level, M=0.3.

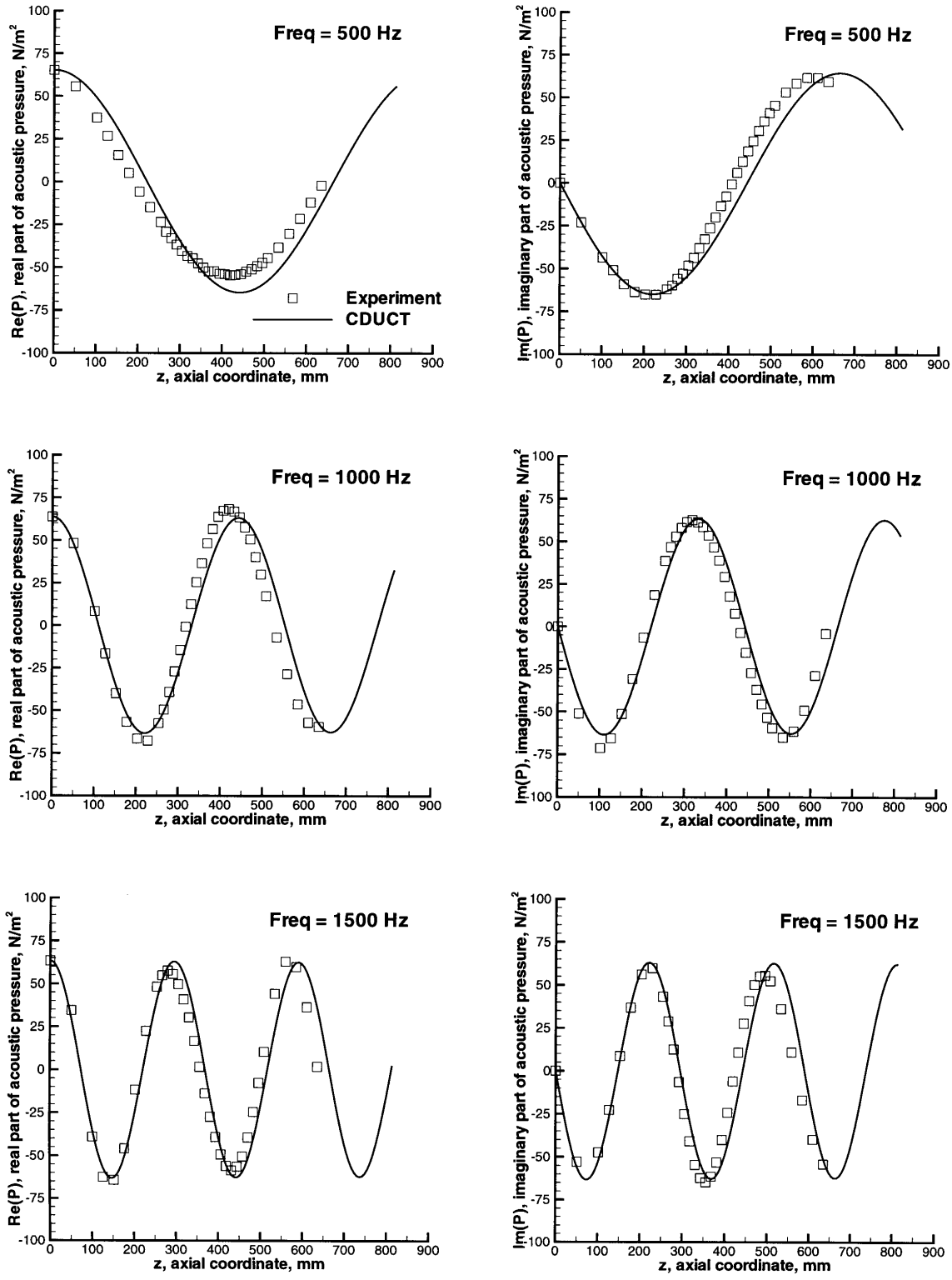

Figure 14. Hardwall real and imaginary parts of acoustic pressure, M=0.3.

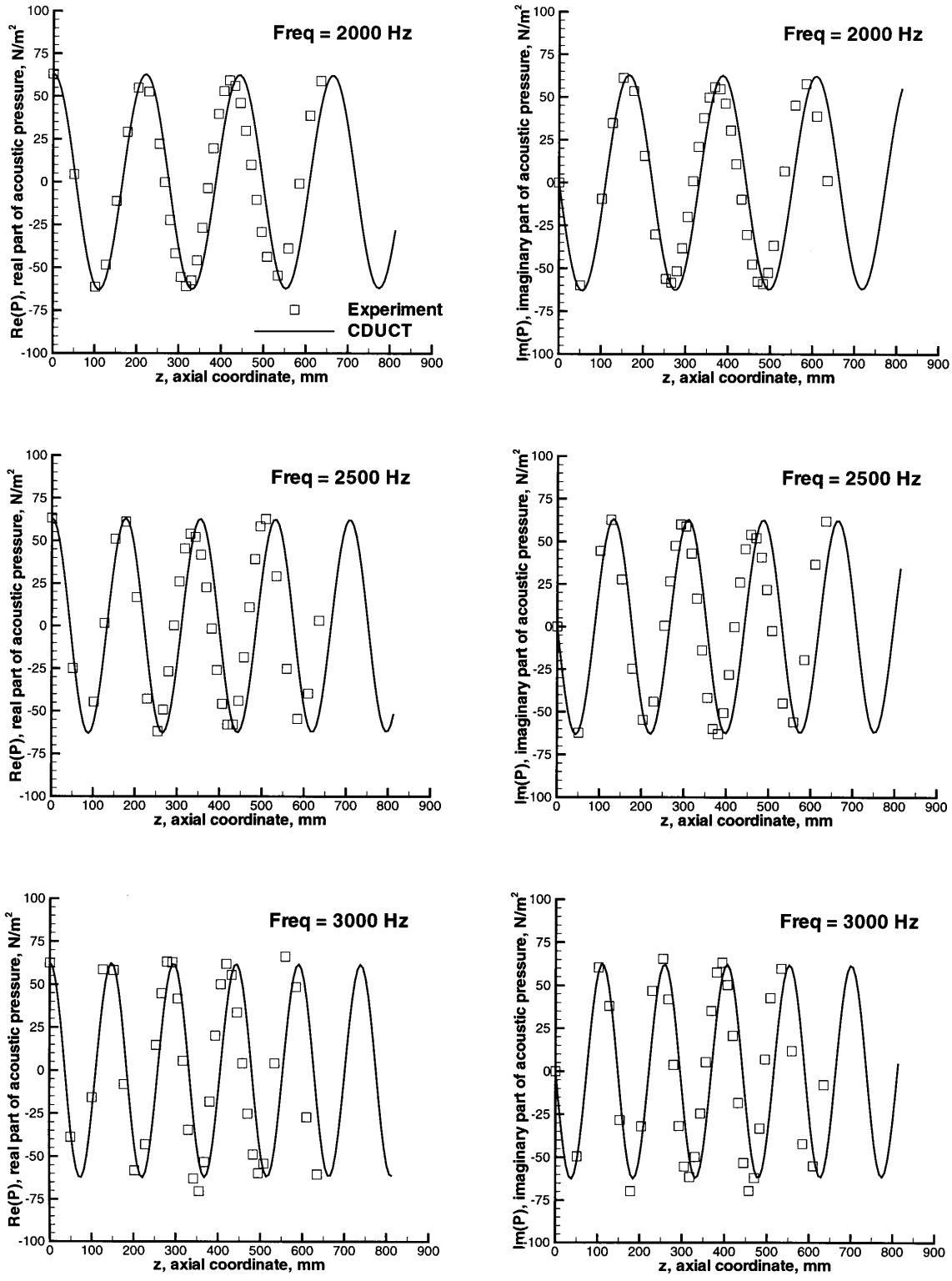

Figure 14. Concluded.

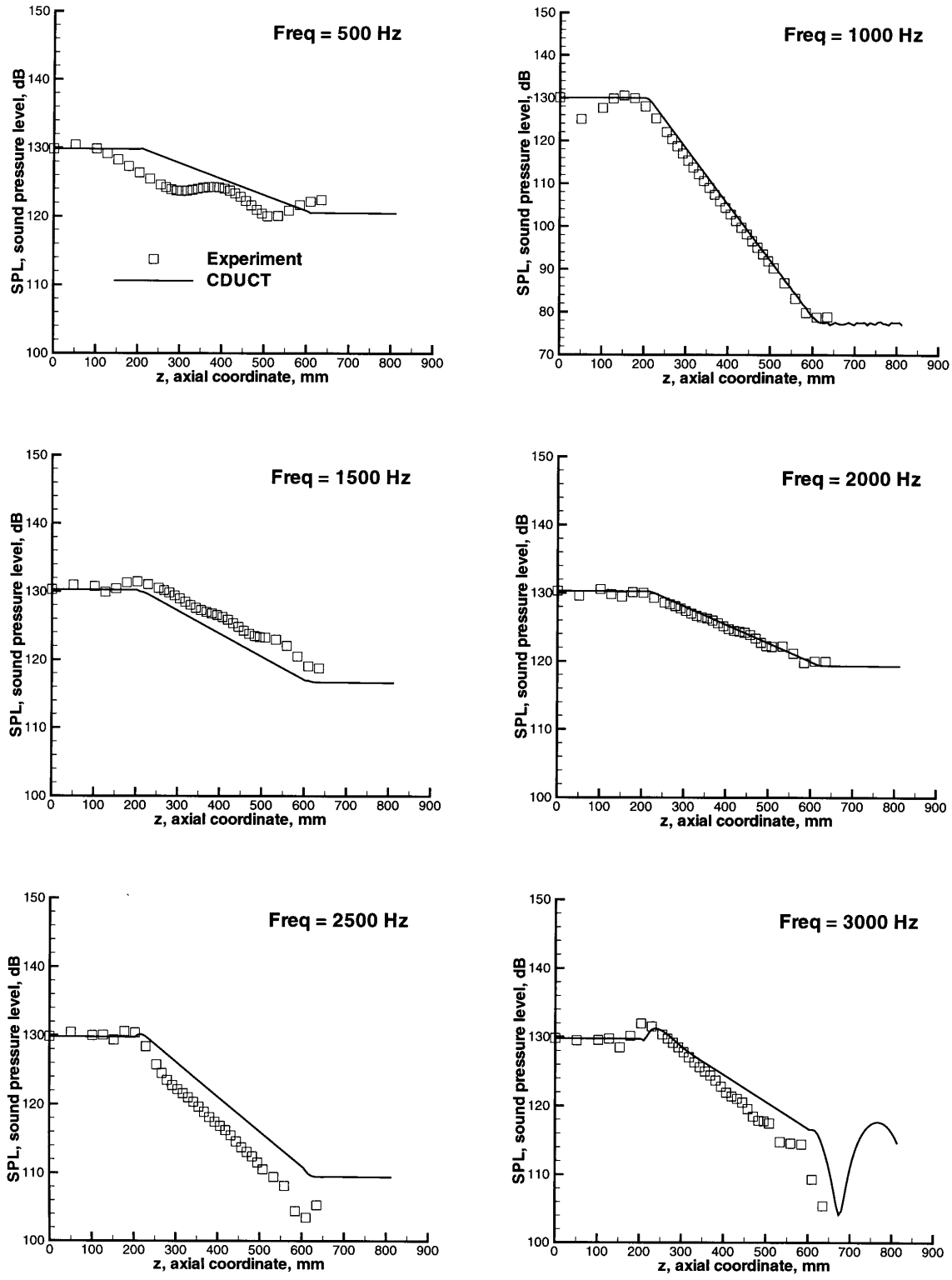

Figure 15. Ceramic tubular liner sound pressure level, M=0.0.

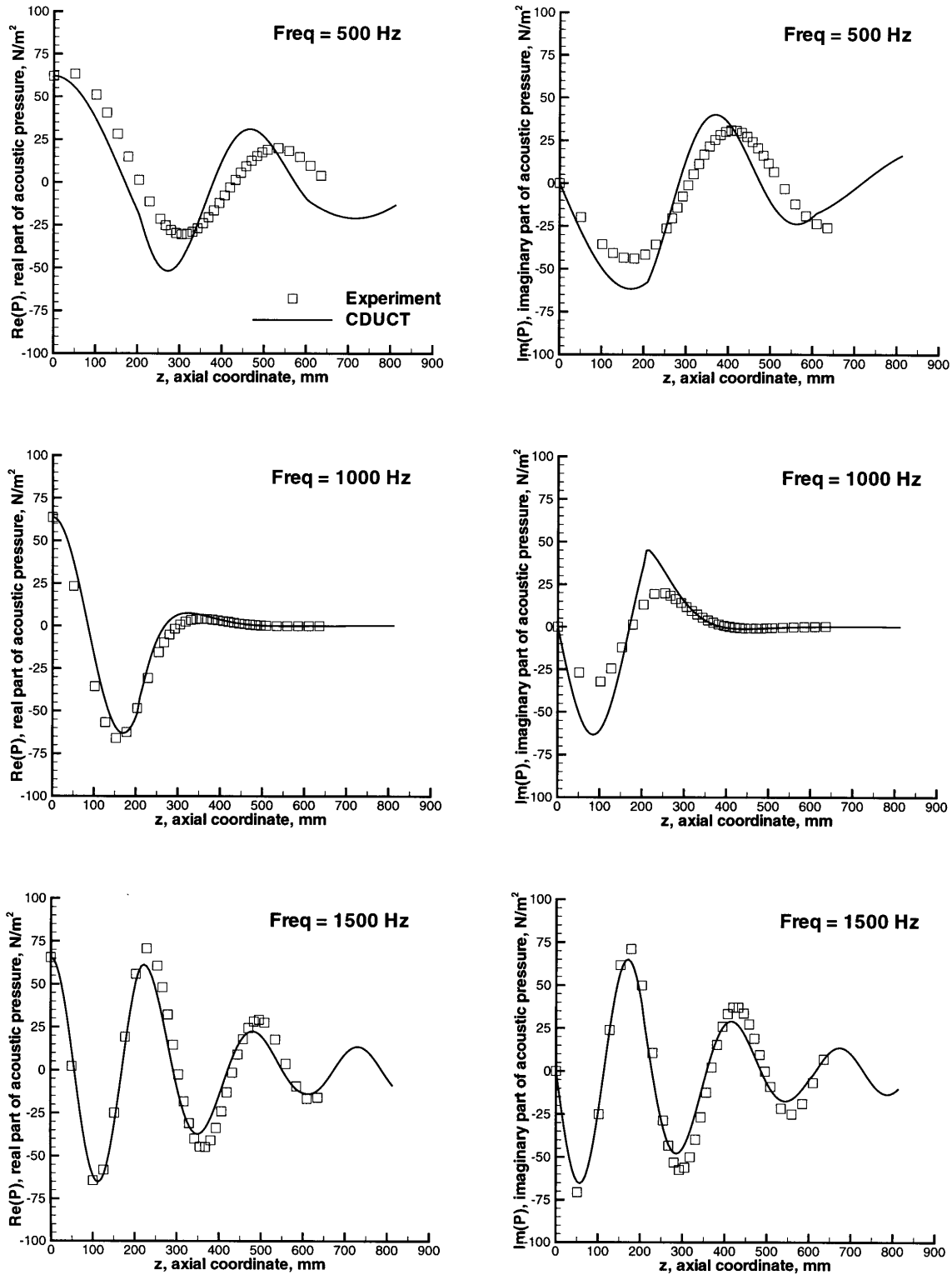

Figure 16. Ceramic tubular liner real and imaginary parts of acoustic pressure, M=0.0.

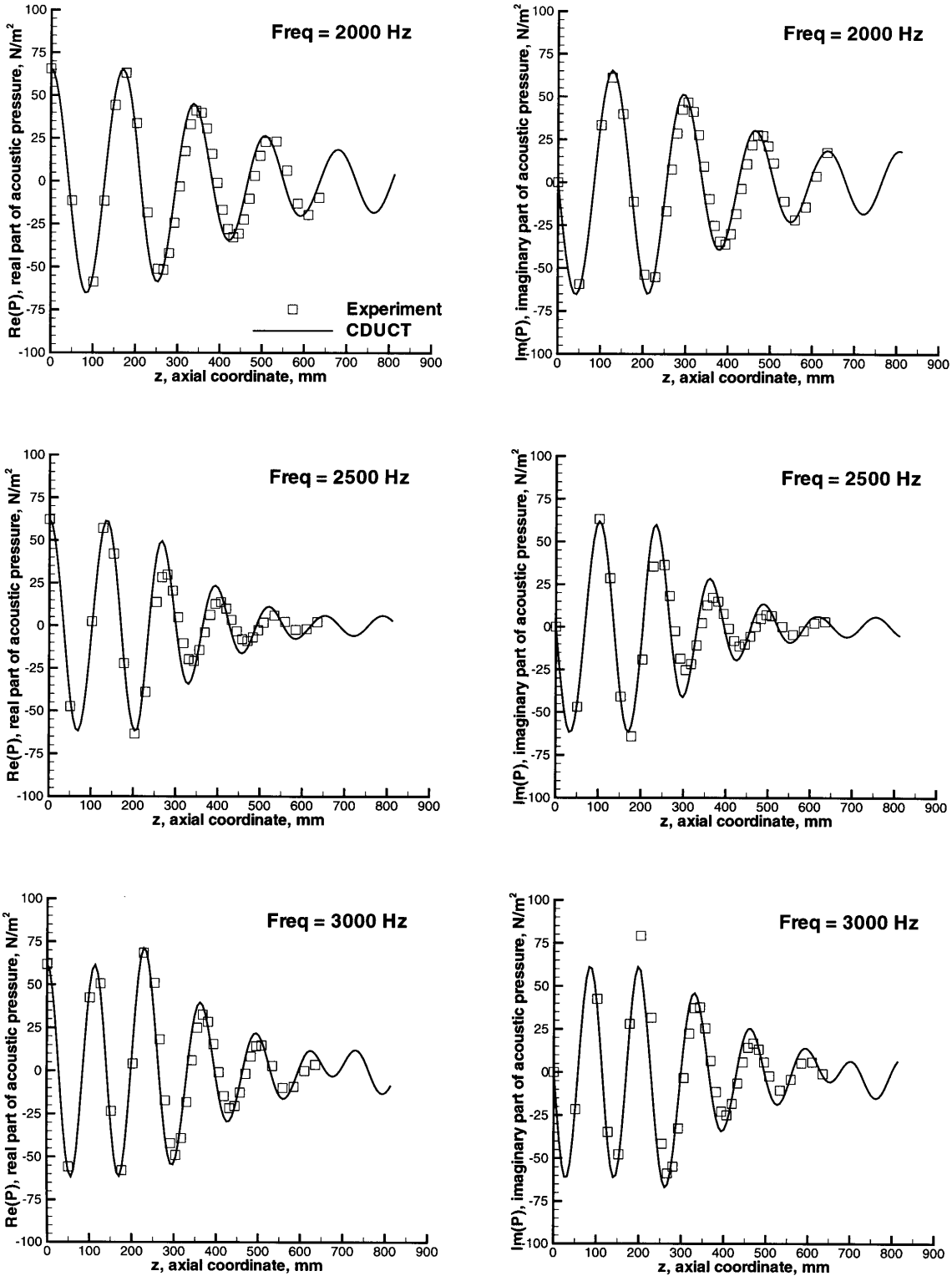

Figure 16. Concluded.

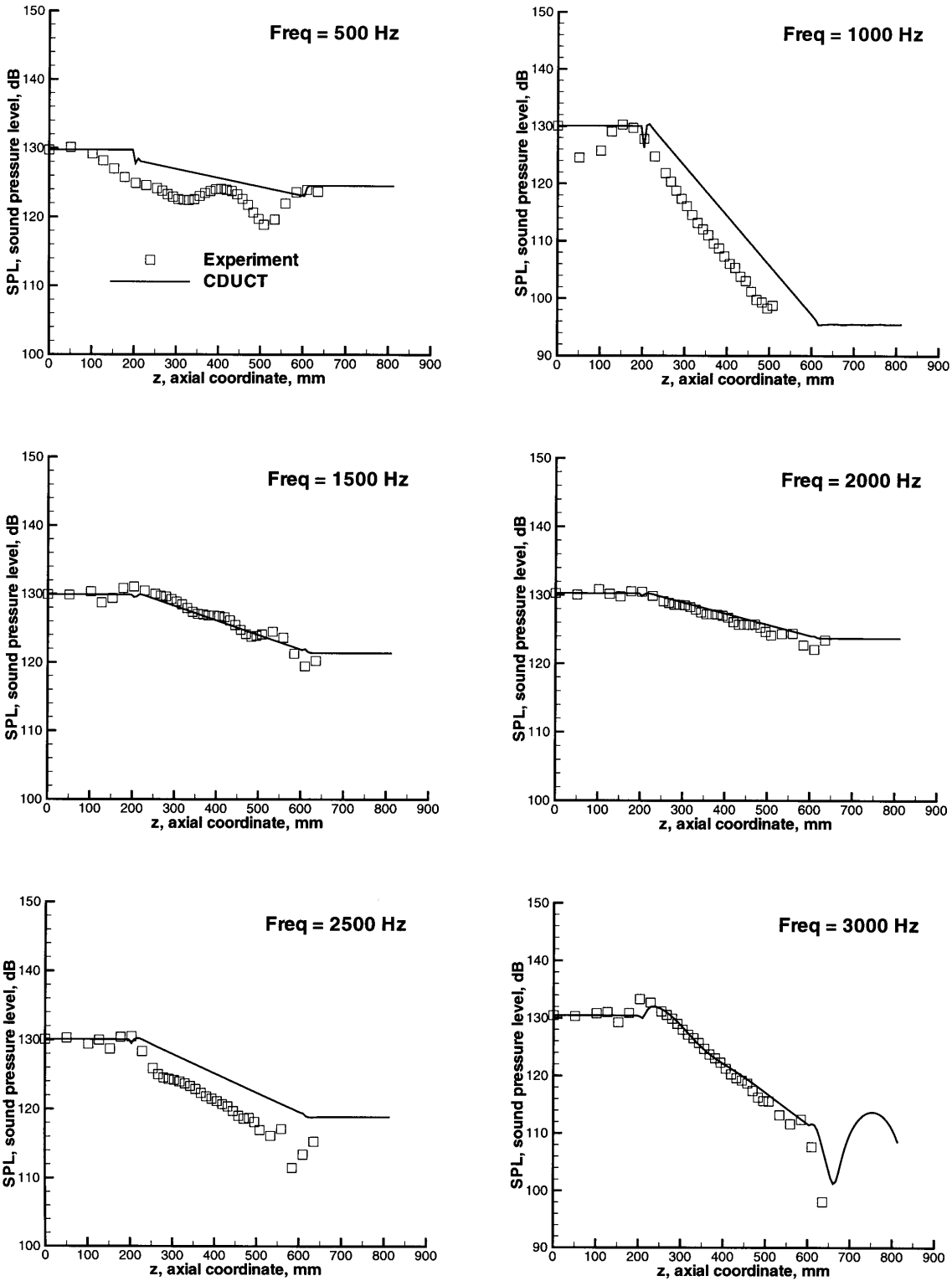

Figure 17. Ceramic tubular liner sound pressure level, M=0.3.

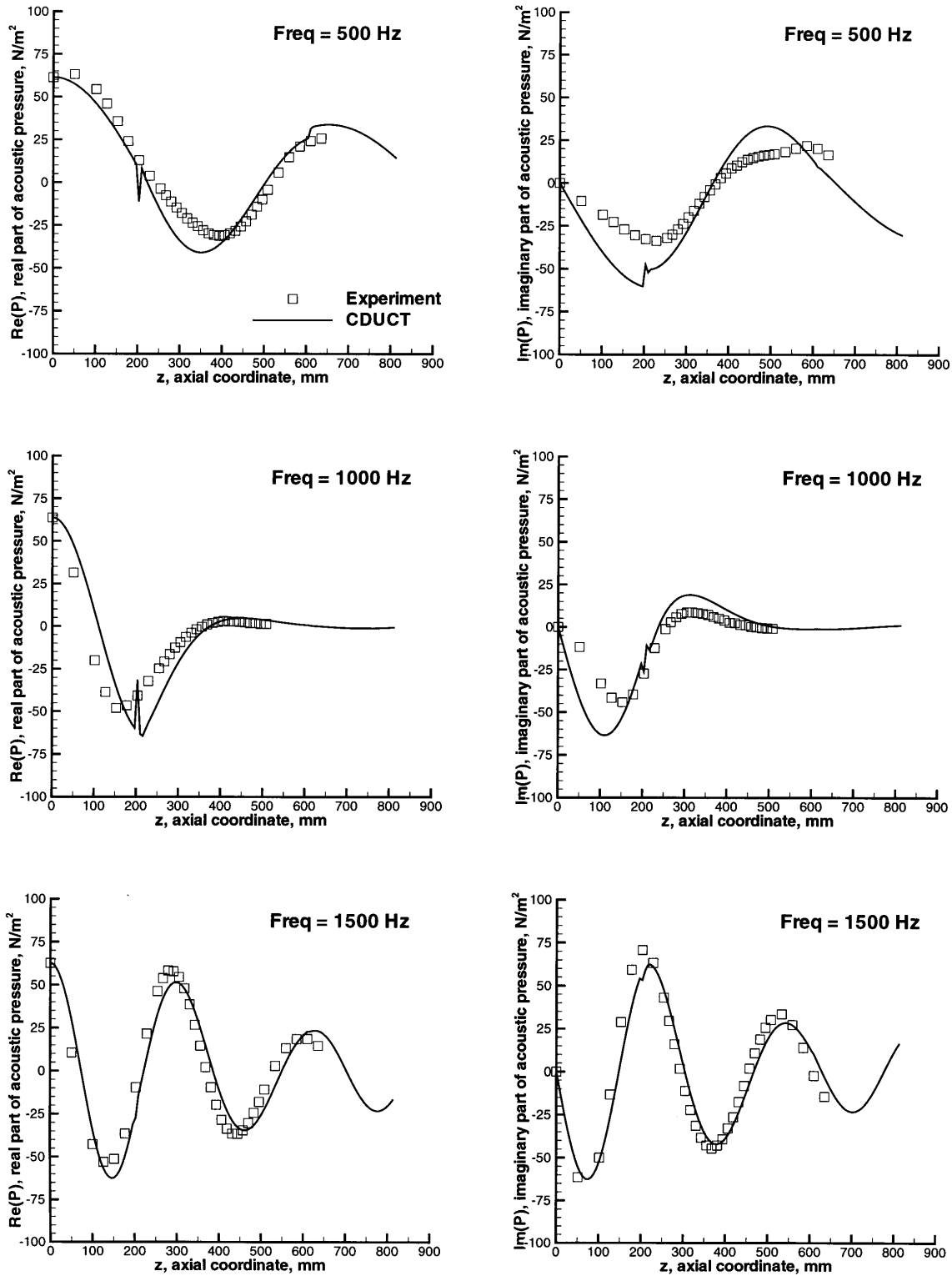

Figure 18. Ceramic tubular liner real and imaginary parts of acoustic pressure, M=0.3.

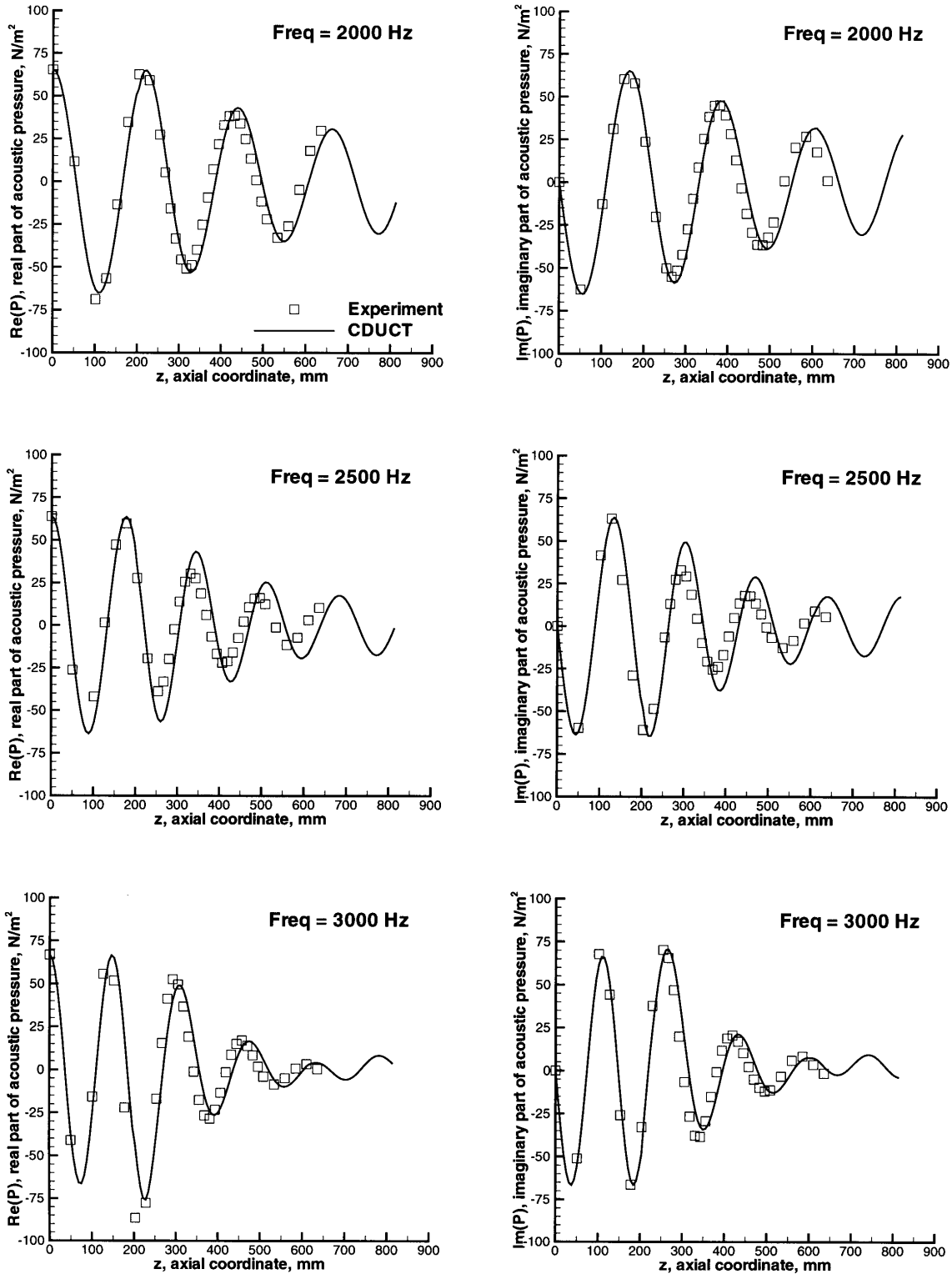

Figure 18. Concluded.

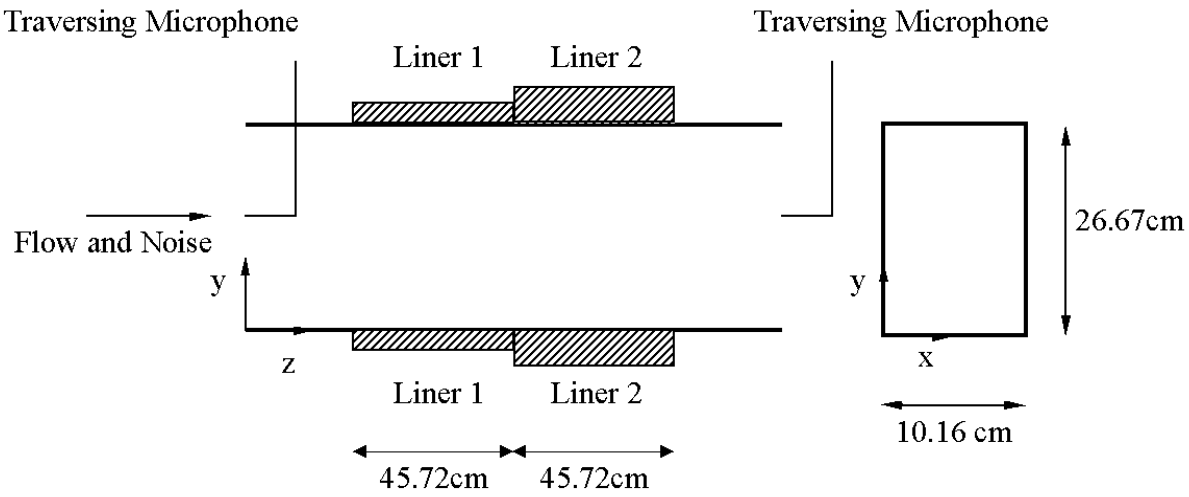

Figure 19. Rectangular flow duct schematic.

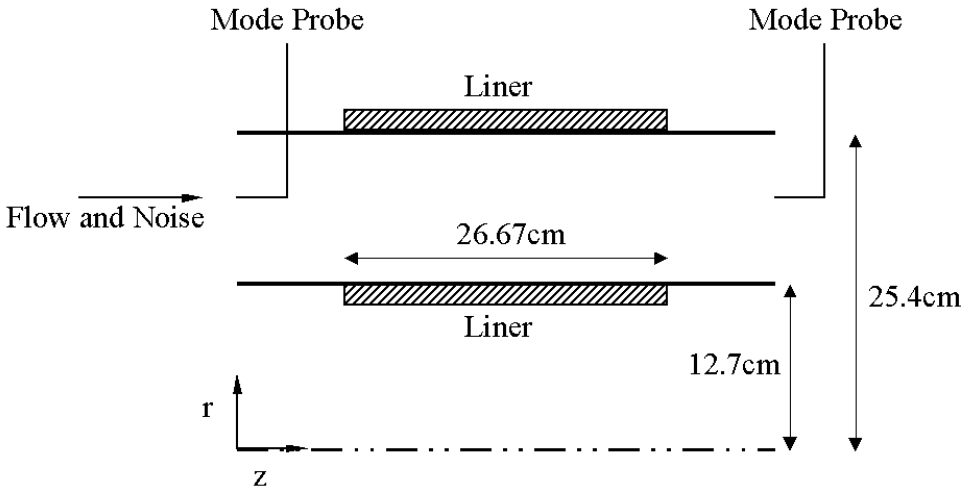

Figure 20. Annular flow duct schematic.

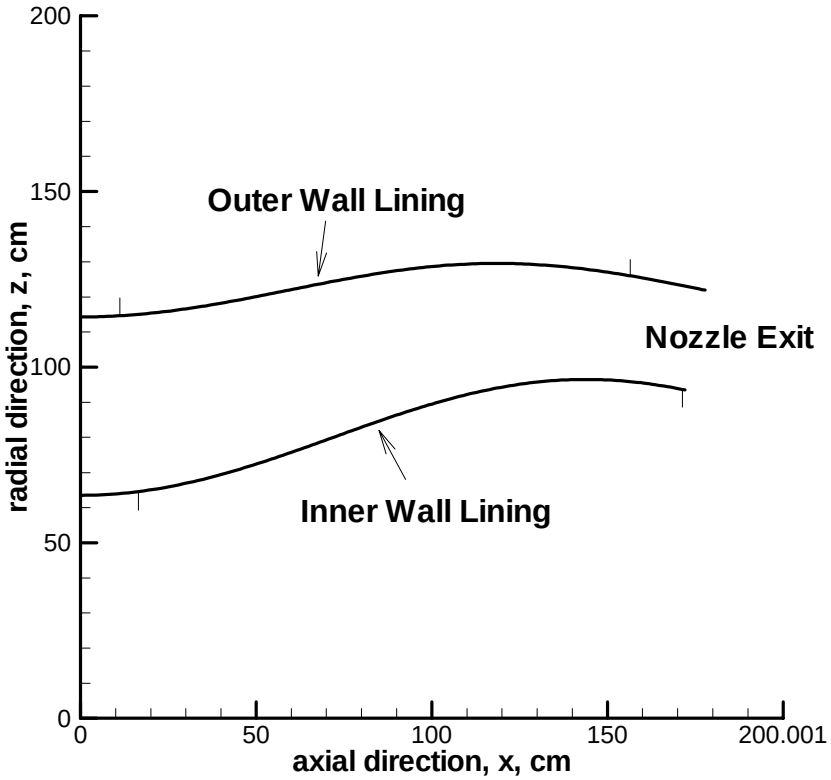

Figure 21. Example aft fan duct geometry.

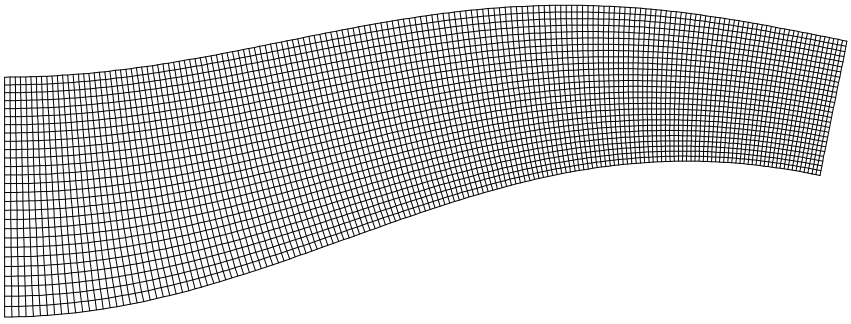

Figure 22. Computational grid for example aft fan duct (28 X 162).

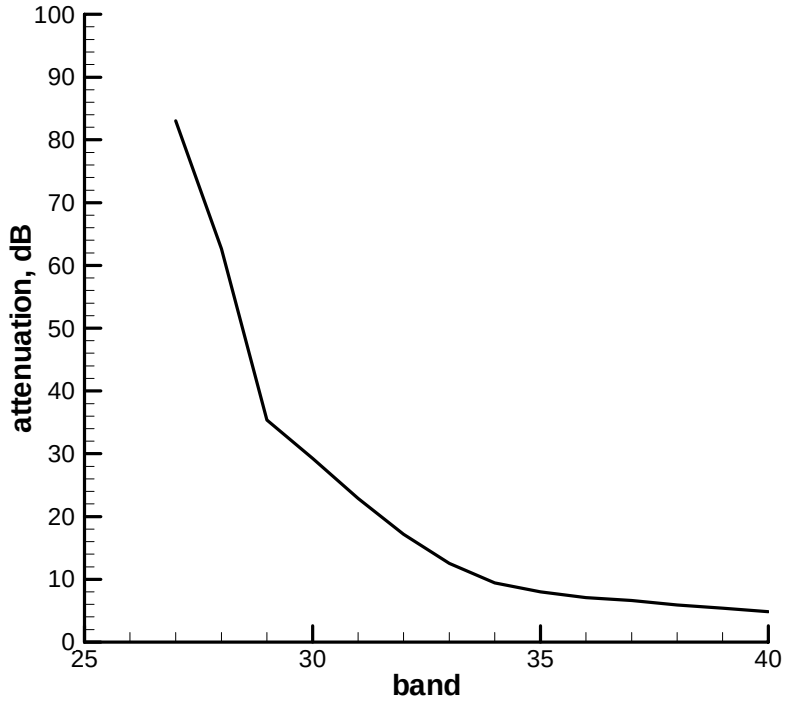

Figure 23. Optimum attenuations for uniform lining.

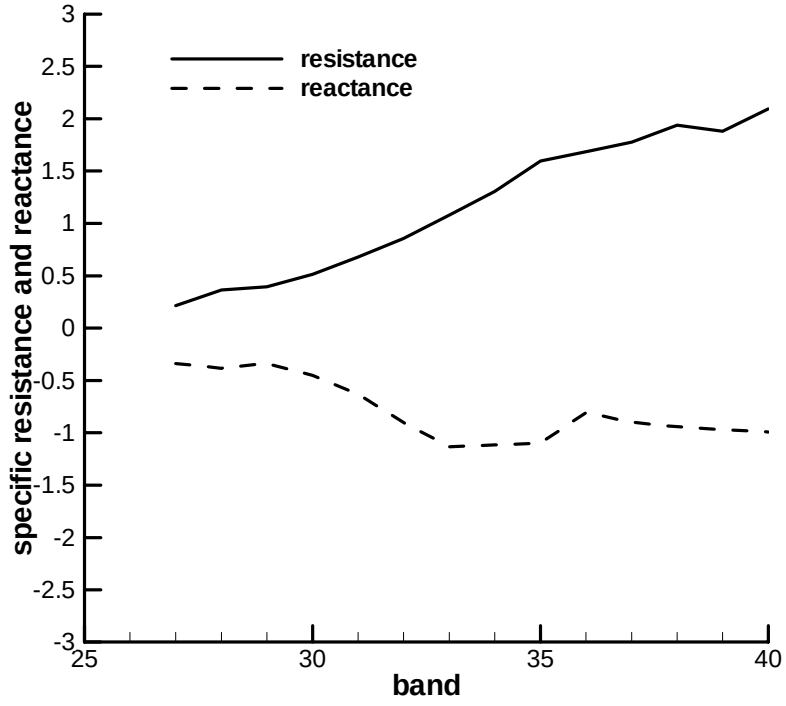

Figure 24. Optimum specific resistance and reactance for uniform lining.

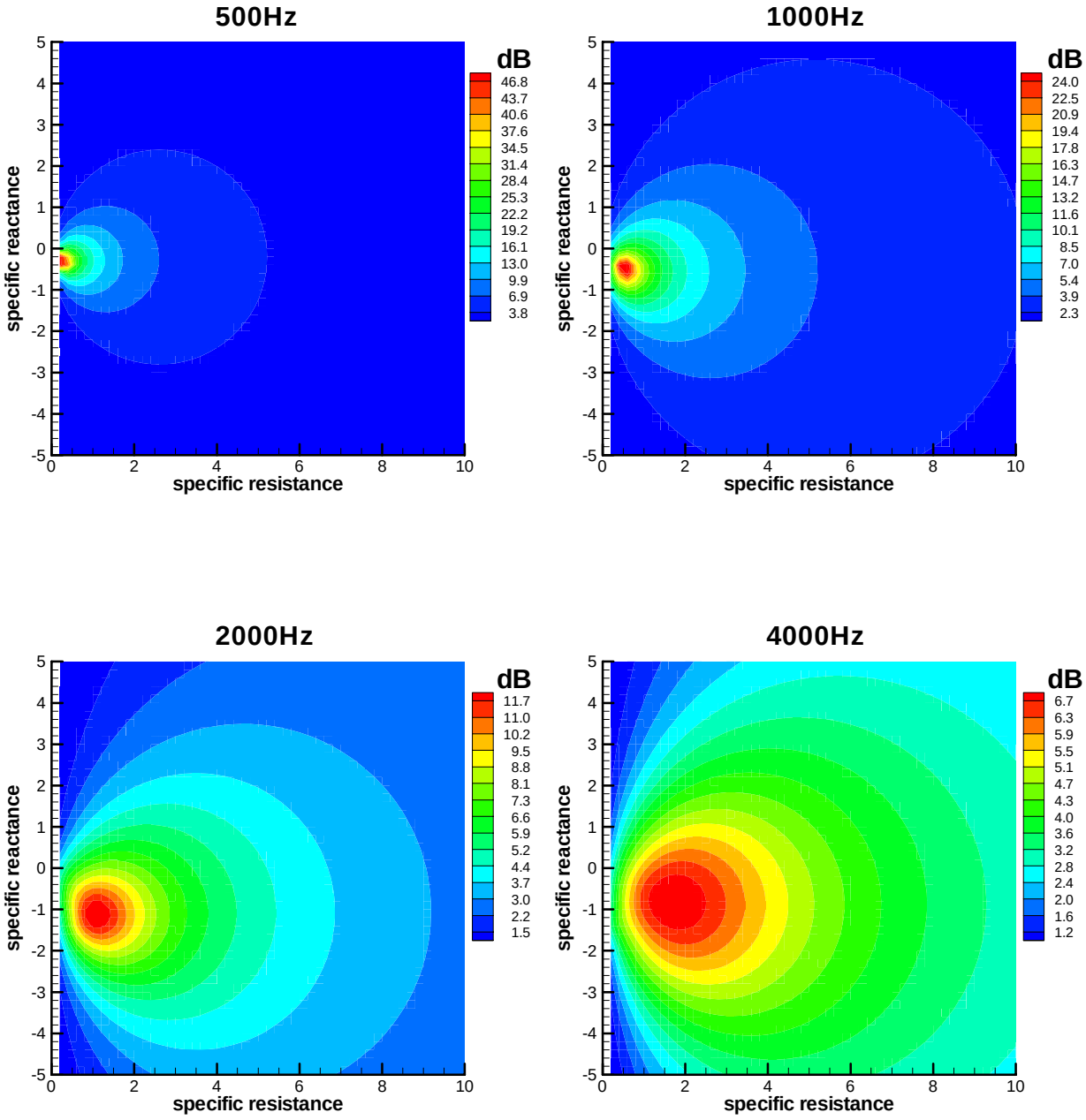

Figure 25. Attenuation contours for 500Hz, 1000Hz, 2000Hz, 4000Hz.

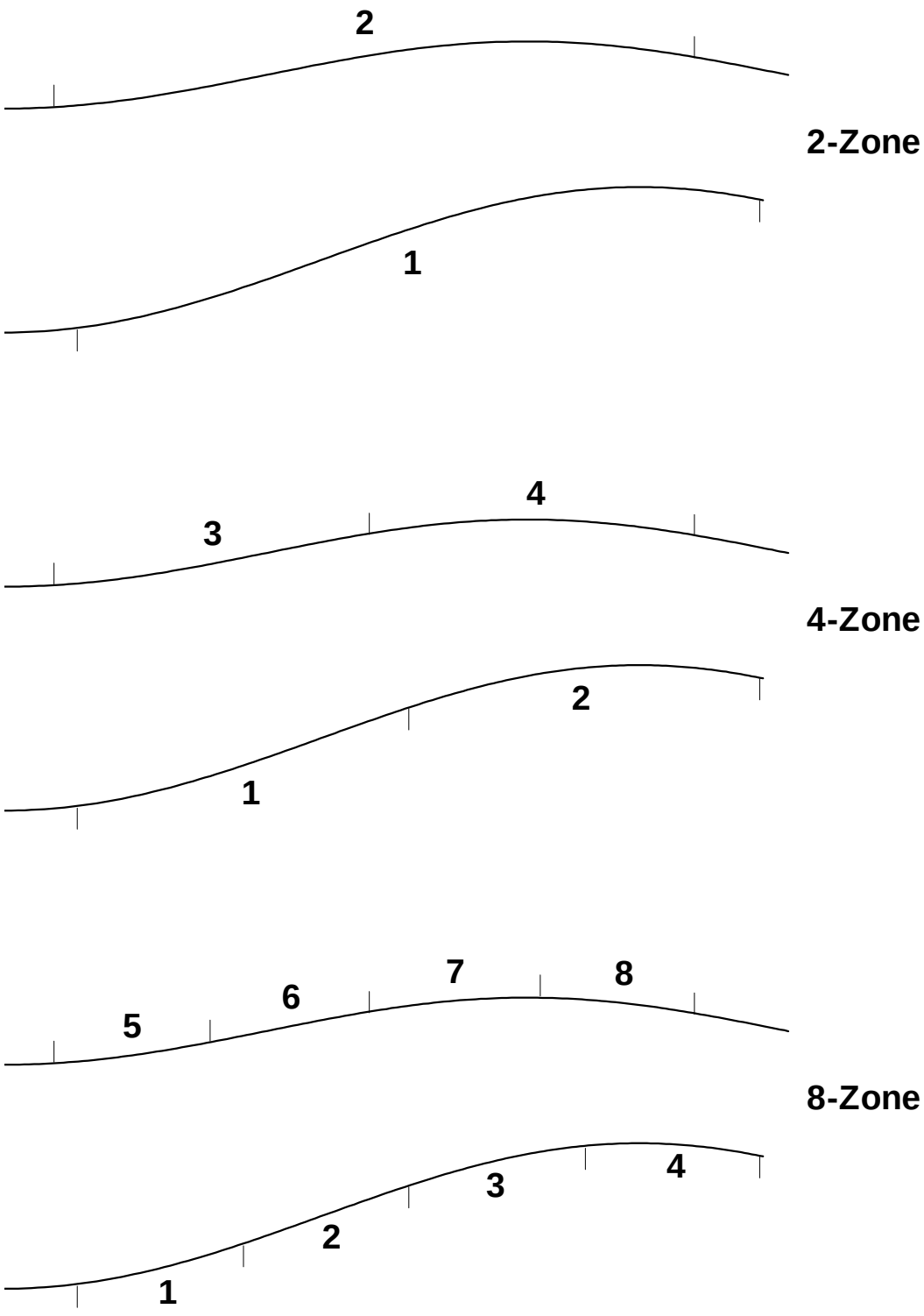

Figure 26. Segmented acoustic lining envelope.

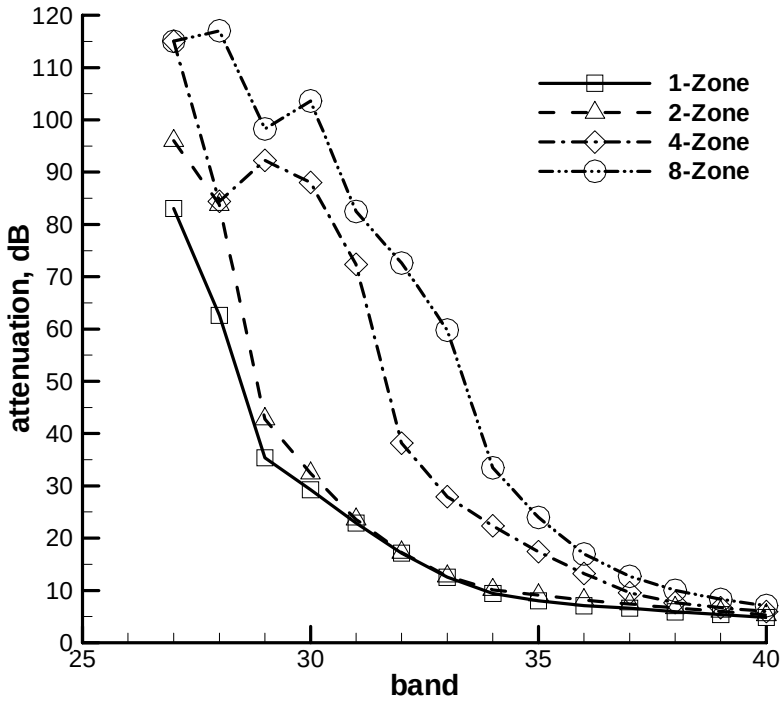

Figure 27. Optimum attenuations for 1, 2, 4, 8-Zone cases.

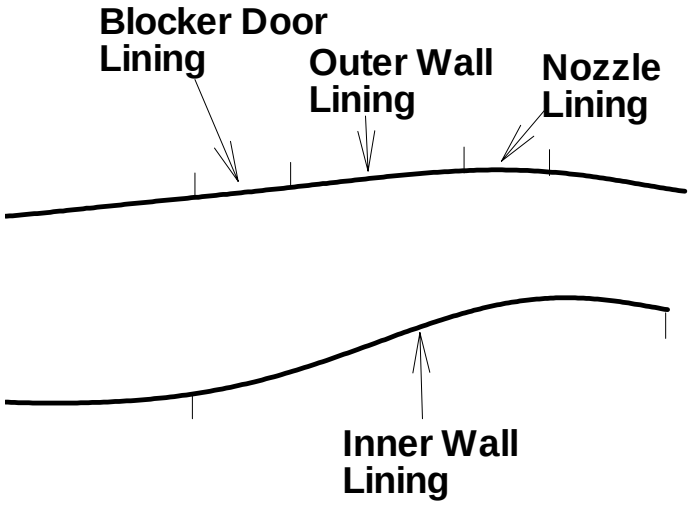

Figure 28. Example aft fan duct geometry for lining design.

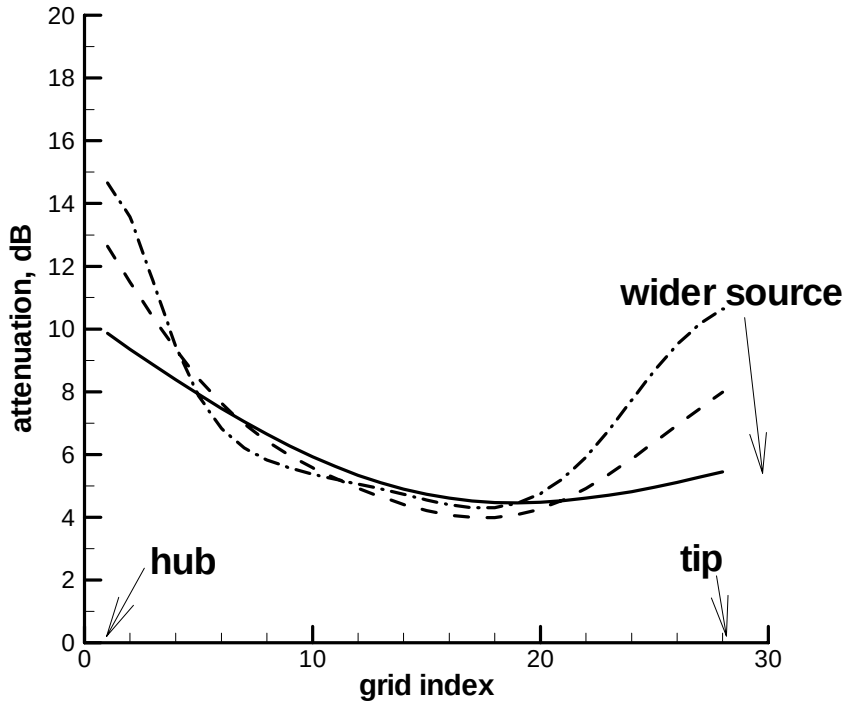

Figure 29. Attenuation for various radial positions of three Gaussian sources.

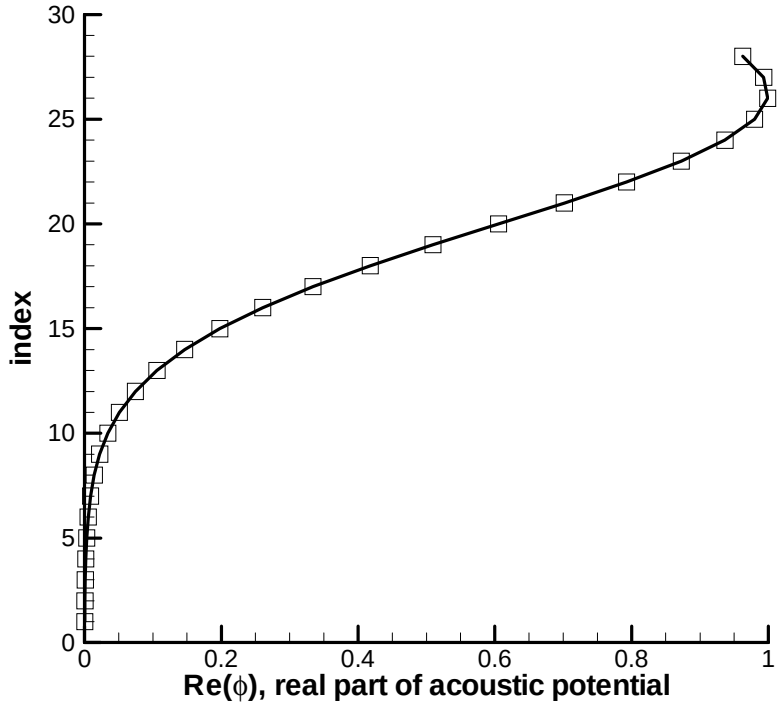

Figure 30. Gaussian tip source.

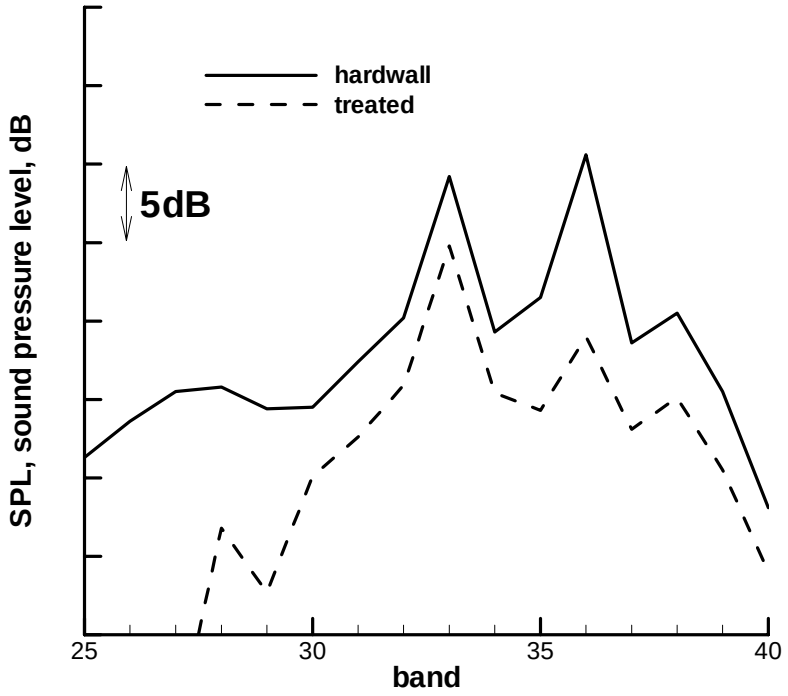

Figure 31. Hardwall and treated spectra for narrow-chord turbofan engine.

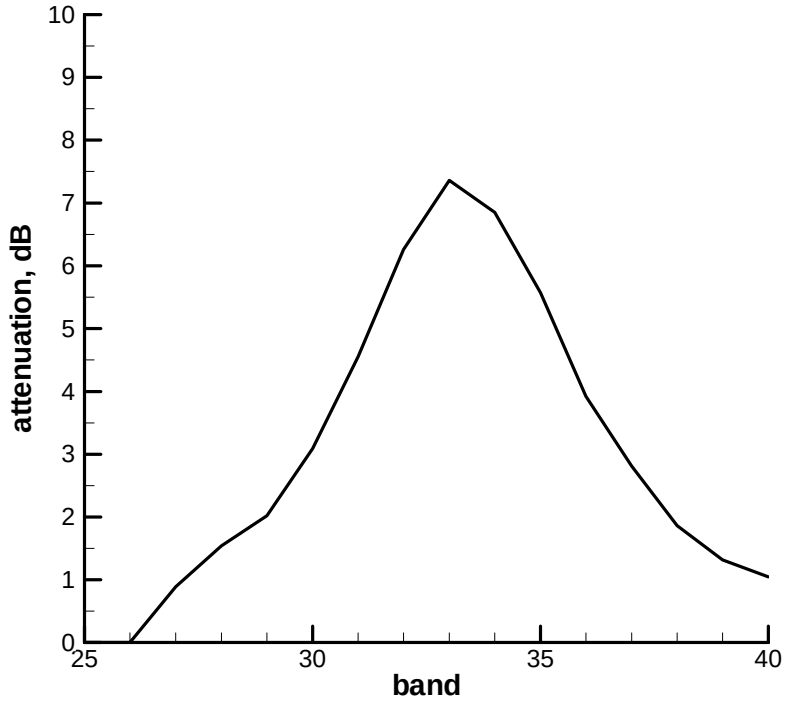

Figure 32. CDUCT calculated attenuation for baseline lining, Gaussian tip source, conventional geometry.

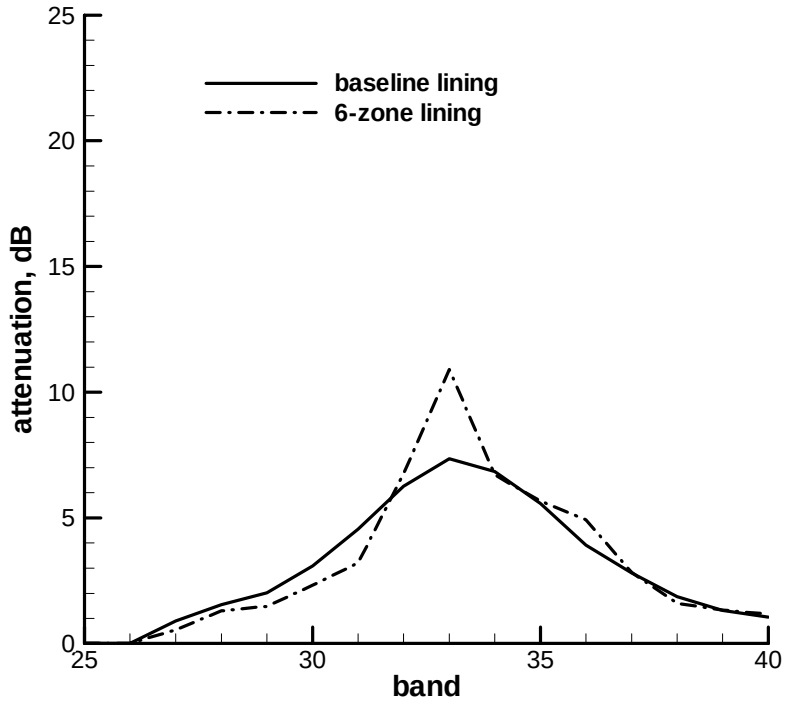

Figure 33. CDUCT calculated attenuation in conventional geometry, baseline and 6-zone lining.

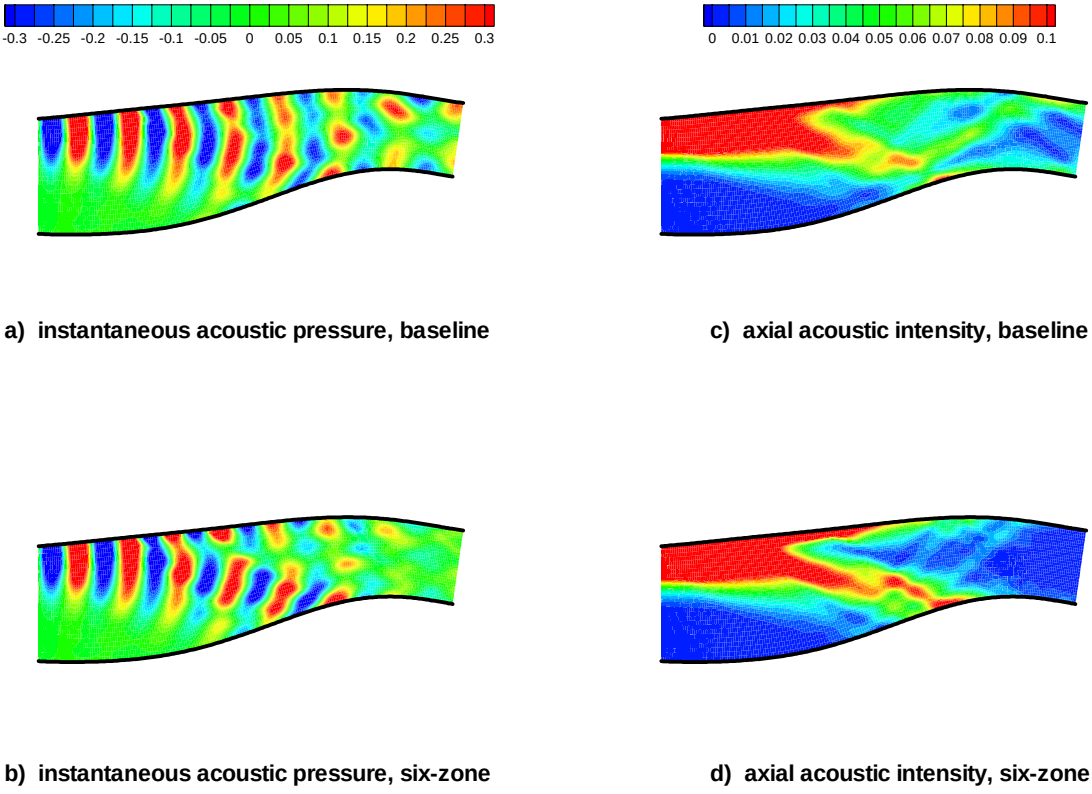

Figure 34. Conventional aft fan duct, 2kHz: a) acoustic pressure, baseline lining, b) acoustic pressure, 6-zone lining, c) axial intensity, baseline lining, d) axial intensity, 6-zone lining.

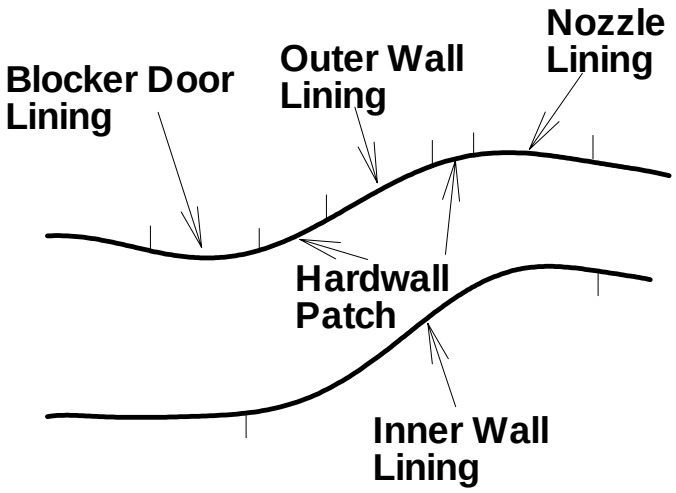

Figure 35. Highly curved aft fan duct geometry.

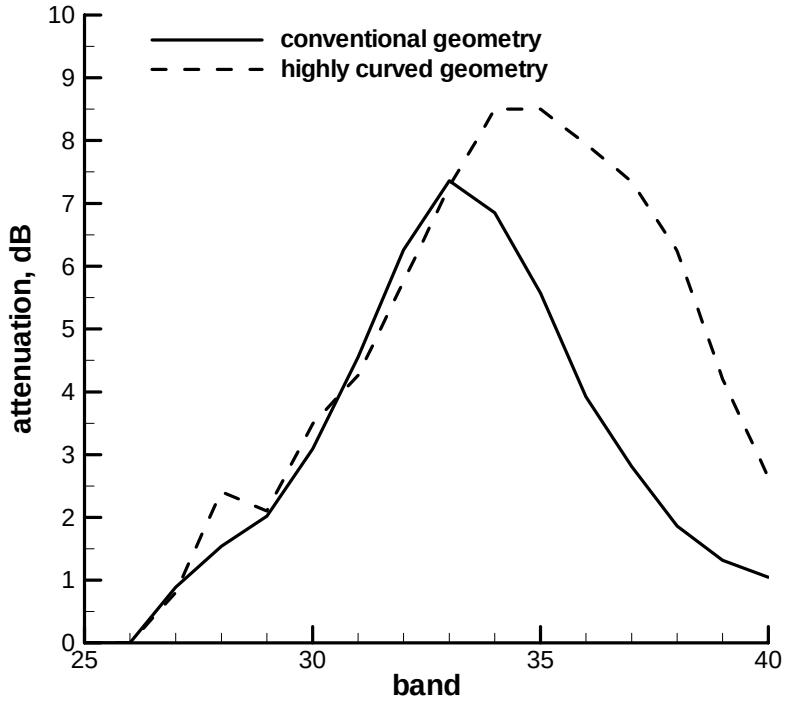

Figure 36. CDUCT calculated attenuation in conventional and highly curved geometry, Gaussian tip source, baseline lining.

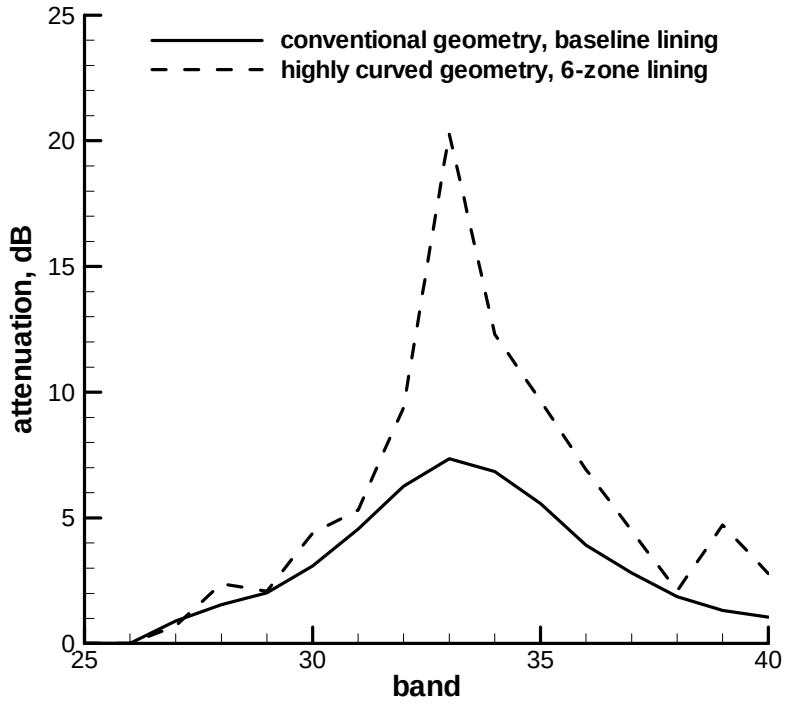

Figure 37. CDUCT calculated attenuation in conventional geometry with baseline lining and highly curved geometry with 6-zone lining.

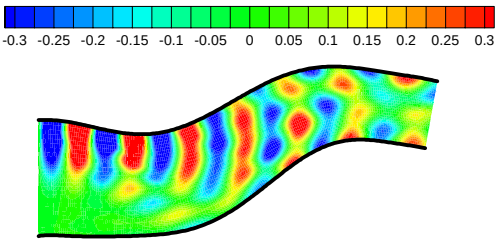

a) instantaneous acoustic pressure, baseline

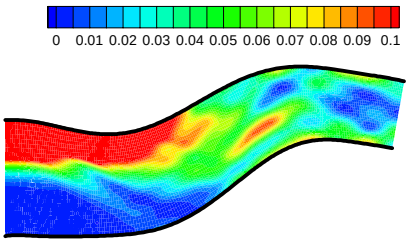

c) axial acoustic intensity, baseline

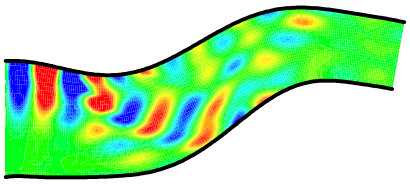

b) instantaneous acoustic pressure, six-zone

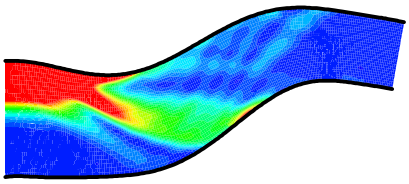

d) axial acoustic intensity, six-zone

Figure 38. Highly curved aft fan duct, 2kHz: a) acoustic pressure, baseline lining, b) acoustic pressure, 6-zone lining, c) axial intensity, baseline lining, d) axial intensity, 6-zone lining.

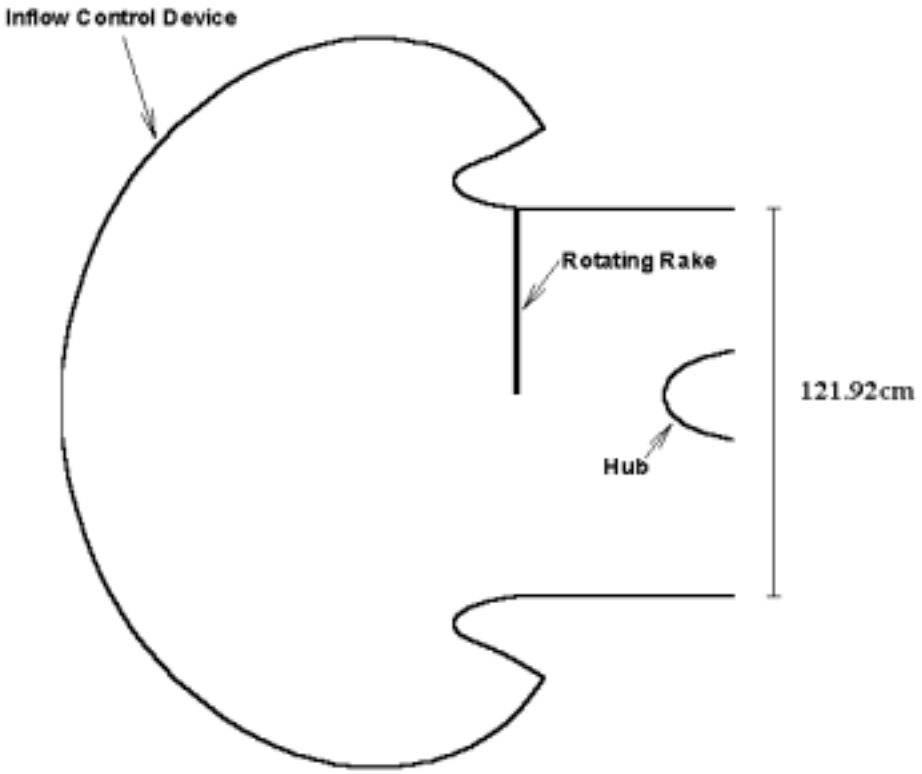

Figure 39. Schematic of ANCF facility.

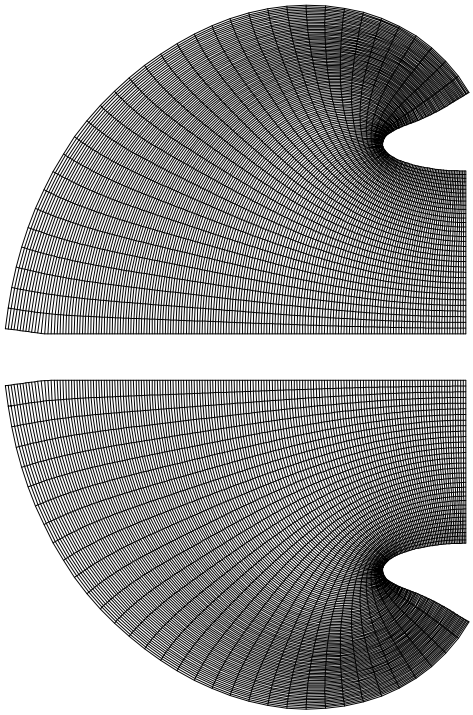

Figure 40. Computational grid for ANCF facility.

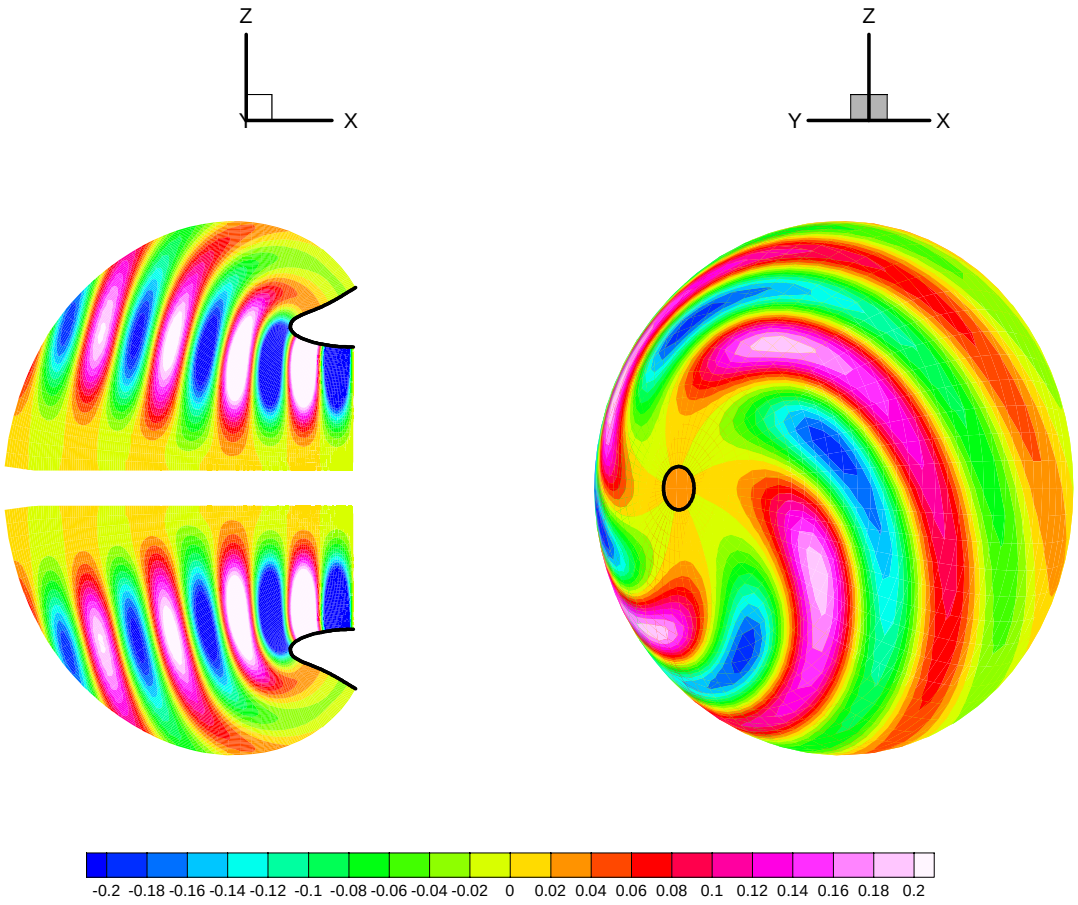

Figure 41. Sample CDUCT solution for ANCF, (-4,0) mode, 2BPF.

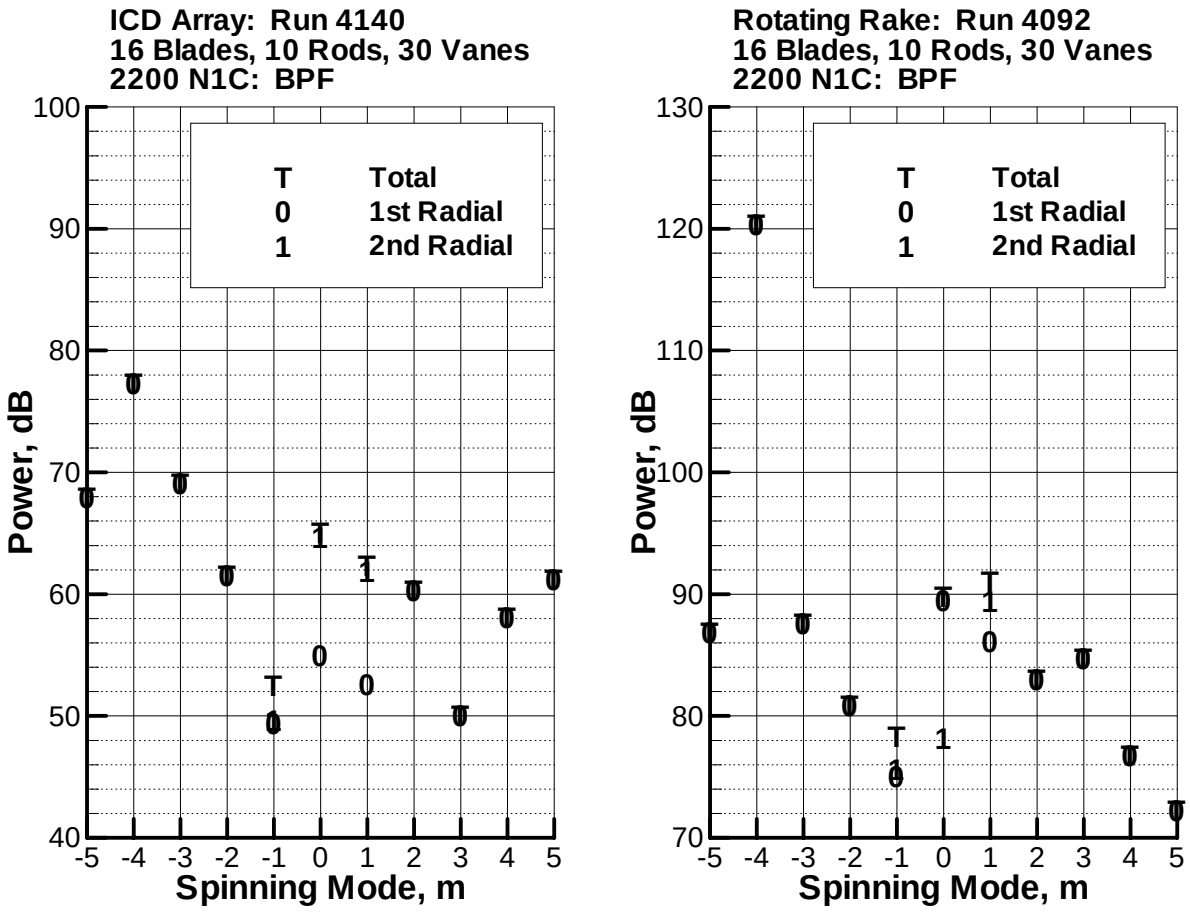

Figure 42. Comparison between ICD array and rotating rake, 10 rods, BPF.

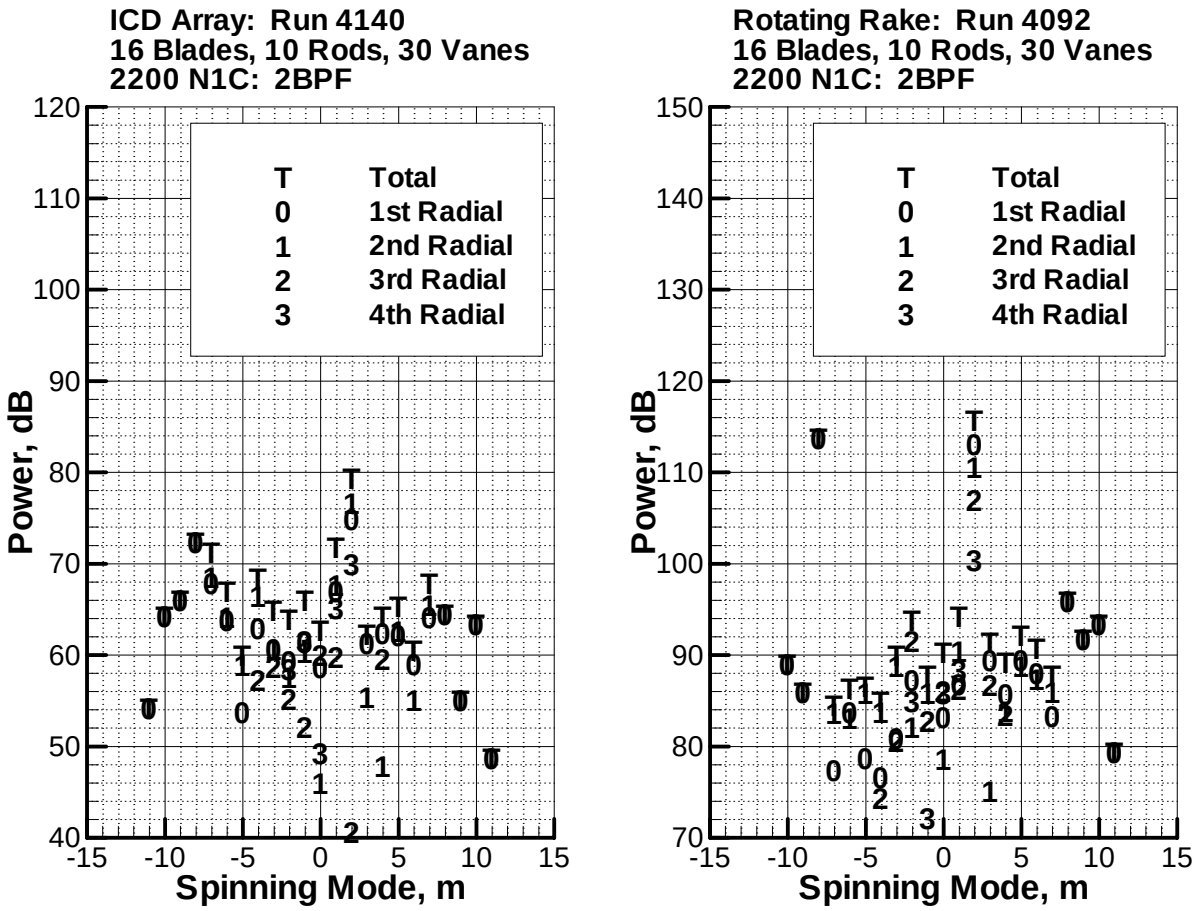

Figure 43. Comparison between ICD array and rotating rake, 10 rods, 2BPF.

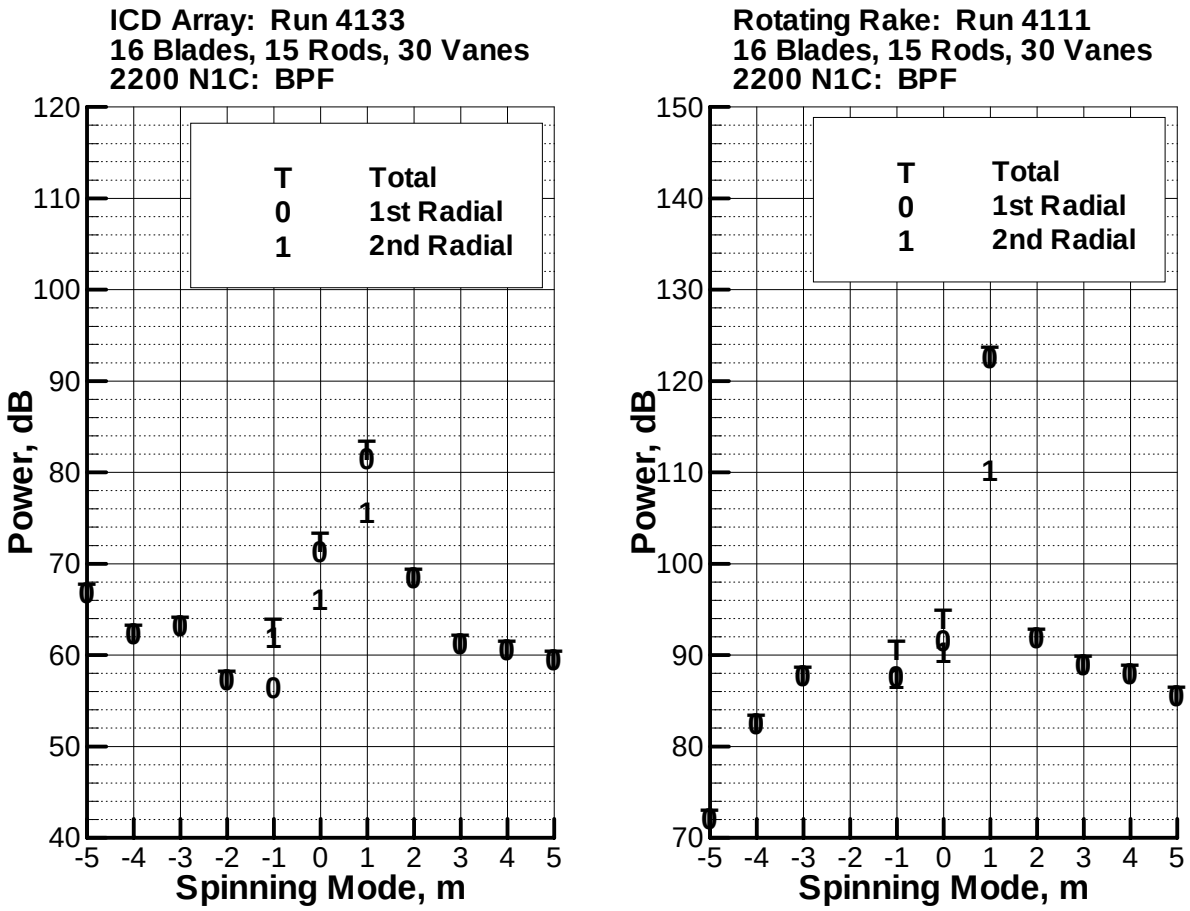

Figure 44. Comparison between ICD array and rotating rake, 15 rods, BPF.

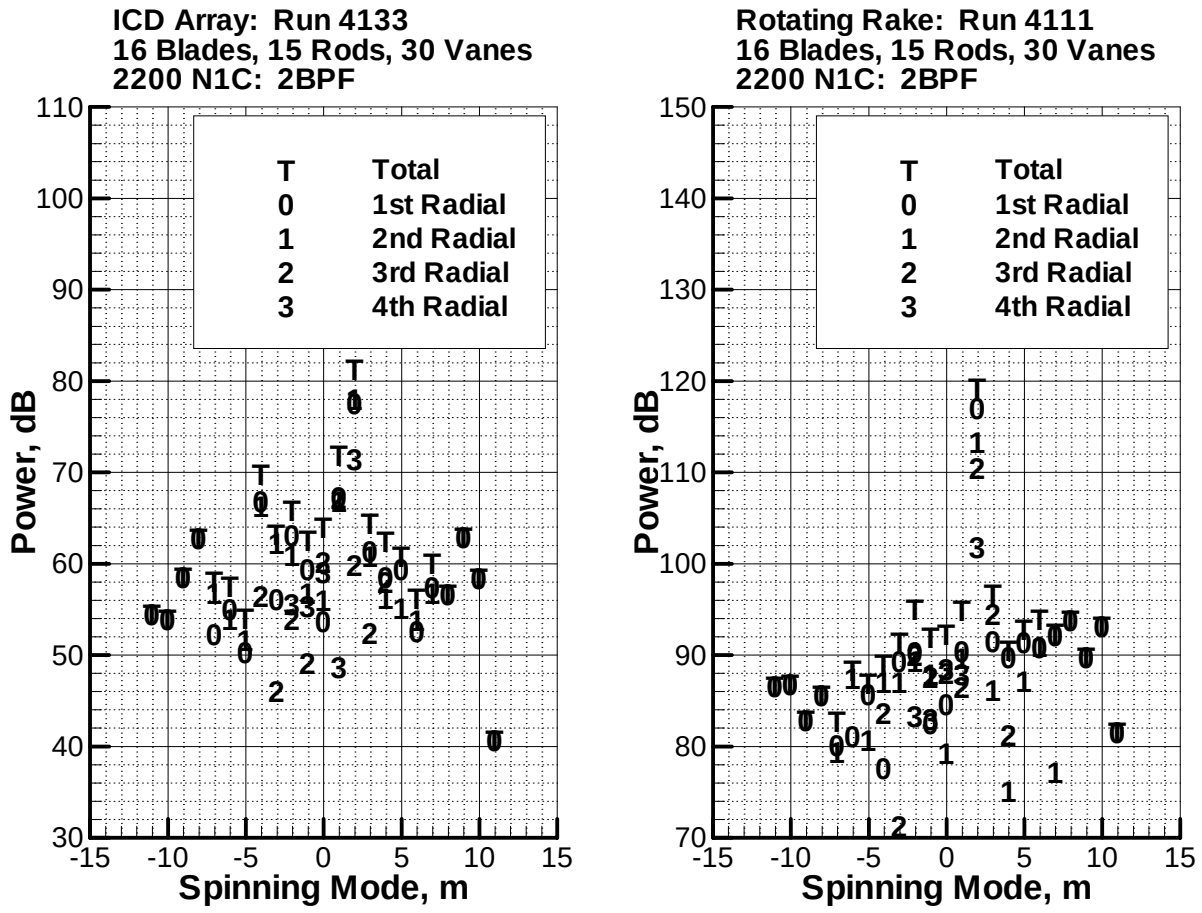

Figure 45. Comparison between ICD array and rotating rake, 15 rods, 2BPF.

REPORT DOCUMENTATION PAGE

Form Approved
OMB No. 0704-0188

1. AGENCY USE ONLY (*Leave blank*)	2. REPORT DATE	3. REPORT TYPE AND DATES COVERED
	December 2001	Contractor Report

4. TITLE AND SUBTITLE
Turbofan Duct Propagation Model

5. FUNDING NUMBERS
NAS1-97040
Task 5
WU 706-81-12-01

6. AUTHOR(S)
Justin H. Lan

7. PERFORMING ORGANIZATION NAME(S) AND ADDRESS(ES)
The Boeing Company
Acoustics and Fluid Mechanics
P.O. Box 3707 MS 67-ML
Seattle, WA 98124

8. PERFORMING ORGANIZATION REPORT NUMBER

9. SPONSORING/MONITORING AGENCY NAME(S) AND ADDRESS(ES)
National Aeronautics and Space Administration
Langley Research Center
Hampton, VA 23681-2199

10. SPONSORING/MONITORING AGENCY REPORT NUMBER
NASA/CR-2001-211245

11. SUPPLEMENTARY NOTES
Langley Technical Monitor: Joe W. Posey

12a. DISTRIBUTION/AVAILABILITY STATEMENT
Unclassified-Unlimited
Subject Category 71 Distribution: Standard
Availability: NASA CASI (301) 621-0390

12b. DISTRIBUTION CODE

13. ABSTRACT *(Maximum 200 words)*

The CDUCT code utilizes a parabolic approximation to the convected Helmholtz equation in order to efficiently model acoustic propagation in acoustically treated, complex shaped ducts. The parabolic approximation solves one-way wave propagation with a marching method which neglects backwards reflected waves. The derivation of the parabolic approximation is presented. Several code validation cases are given. An acoustic lining design process for an example aft fan duct is discussed. It is noted that the method can efficiently model realistic three-dimension effects, acoustic lining, and flow within the computational capabilities of a typical computer workstation.

14. SUBJECT TERMS
duct propagation, acoustic lining, parabolic approximation, turbofan

15. NUMBER OF PAGES
71

16. PRICE CODE

17. SECURITY CLASSIFICATION OF REPORT	18. SECURITY CLASSIFICATION OF THIS PAGE	19. SECURITY CLASSIFICATION OF ABSTRACT	20. LIMITATION OF ABSTRACT
Unclassified	Unclassified	Unclassified	UL